

Accepted September 14th 2023

TURBULENT LORENTZ HEAT FLOW VISUALIZATION IN RADIATIVE BOUNDARY LAYER REGIME

S.P. Suresha¹, G Janardhana Reddy^{1,*}, B. Sreenivasulu¹ and O. Anwar Bég²

¹*Laboratory on Computational Fluid Dynamics, Department of Mathematics, Central University of Karnataka, Kalaburagi-585367, India.*

²*Professor, Multi-physical Engineering Sciences, Aeronautical/ Mechanical Engineering Department, School of Science, Engineering and Environment, Salford University, Manchester M54WT, UK.*

*Corresponding author: gjr@cuk.ac.in

Abstract: Modern nuclear energy systems often employ MHD and feature radiative heat transfer. Motivated by studying the near-wall transport phenomena in such applications, the article examines the simultaneous influence of thermal radiative flux and magnetohydrodynamics (MHD) on two-dimensional electrically conducting turbulent flow and natural convective heat transfer about a vertical surface under a transverse static magnetic field using the low Reynolds number (LRN) kinetic energy and dissipation (k - ϵ) model. The Rosseland diffusion flux model is deployed for radiative heat transfer. An optimized Crank-Nicolson finite difference method (FDM) is applied to solve the non-linear and coupled system of Reynolds-averaged boundary layer equations, which includes the equation of average continuity, momentum, energy, kinetic energy, and dissipation rate of kinetic energy. Detailed computations are conducted to visualize the streamlines and heat lines in laminar and turbulent regimes via mathematical stream and heat functions based on the Bejan approach. A detailed parametric study of the effects of the magnetic field, radiative flux and turbulent Reynolds number on flow average velocity, temperature, kinetic energy, and dissipation rate is conducted. The simulations reveal that an increase in the magnetic field intensity (as simulated via the magnetic interaction number) reduces the average velocity and dissipation rate, whereas an increase in thermal radiation decreases the time mean temperature. The study also includes contour plots of kinetic energy and dissipation rate, along with skin friction coefficient and Nusselt number. The obtained numerical outcomes are compared to previous literature, and a good agreement is found. The investigation provides a comprehensive insight into coupled MHD radiative turbulent natural convection flows and a solid benchmark which may further be generalized to three-dimensional simulations.

Keywords: *Magnetic field, Vertical plate, turbulence; k - ϵ model, Thermal radiation, Low Reynolds number, Free convection; Bejan heatline visualization; nuclear engineering.*

Nomenclature:

x : Axial coordinate in the mean flow path

y : Horizontal coordinate normal to the isothermal plate

X : Dimensionless axial coordinate in the mean flow path

Y : Dimensionless horizontal coordinate normal to the isothermal plate

\bar{u} , \bar{v} : Time average velocities along x and y directions, respectively

τ_w : $\mu \left(\frac{\partial \bar{u}}{\partial y} \right) - \rho \overline{u'v'}$, is the total wall shear stress of the turbulent flow

U , V : Dimensionless mean flow velocity in the X and Y paths

\bar{T} : Time average energy

T : Nondimensional time mean energy

t' : Time

t : Nondimensional time

g : Gravitational field

Gr_t : Turbulent thermal Grashof parameter

Pr_t : Turbulent Prandtl number

Re_t : Turbulent Reynolds number

M : Magnetic parameter

Nr : Thermal radiation parameter

k^* : Mean absorption coefficient

σ_s : Stefan Boltzmann radiation constant

H : Dimensionless turbulent heat function

\bar{H} : Dimensional turbulent heat function

Ψ : Dimensionless turbulent stream function

C_1, C_2 : Empirical constants

f_1, f_2, f_μ : Damping functions for LRN k- ϵ turbulence model

k : Time average turbulent energy

ϵ : Time average turbulence energy dissipation rate

K : Dimensionless turbulent flow's kinetic energy

E : Dimensionless turbulent energy's dissipation

C_k : Arbitrary Prandtl number-dependent coefficient

C_μ : Proportional constant

K_T : Thermal conductivity

\bar{u}_∞ : Ambient average velocity

C_p : Specific heat capacity at constant pressure

Greek symbols

α_t : Turbulent thermal diffusivity

σ_T, σ_k : Turbulent Prandtl numbers for \bar{T} and k

σ_ϵ : Dissipation Prandtl number

μ : Laminar dynamic viscosity

μ_t : Dynamic viscosity for turbulent flow

ν, ν_t : Laminar and turbulent kinematic viscosities, respectively

$\frac{\nu_t}{\nu}$: Viscosity ratio parameter

ρ : Density

$\beta_{\bar{T}}$: Volumetric thermal expansion coefficient

Subscripts:

l, m : Grid levels in (X, Y) coordinate space

w : Surface condition

∞ : Free stream condition

Superscripts:

n : Time step level

1.Introduction:

Turbulent flows are fundamental to practically every branch of engineering [1] and environmental sciences [2]. These flows are highly chaotic and often feature heat transfer and also mass transfer. All types of vehicles, including automobiles, aeroplanes [3,4], ships, and submarines, exhibit turbulence phenomena in the external flow. Turbulent flow is also a crucial mechanism in natural or free convection that influences the weather by causing large-scale circulation in the atmosphere and bodies of water, such as lakes and oceans, and cools electronic circuit boards in computers [5]. This phenomenon is caused by density gradients and a gravitational field. Furthermore, studying natural convection turbulent flows with different physical and chemical effects has significant applications in diverse areas of science and technology. In the context of nuclear engineering power systems, turbulence is also a significant consideration. To control the temperatures and regulate complex duct flows, MHD (magnetohydrodynamics) is often deployed. This involves the interaction of externally applied magnetic fields and electro-conductive fluids such as potassium and sodium-water solutions which arise in nuclear reactors. Many components of modern nuclear reactors feature MHD turbulence including liquid metal [6], lithium blankets in fusion reactors [7], flow-couplers for

fast breeder reactors [8, 9], thermal mixing argumentation and flow damping mechanisms for experimental fusion reactors [10] and divertors in helical reactors [11]. Further applications of MHD turbulent flows include pumping, stirring and levitation devices for liquid metals. Another important consideration in nuclear power systems is high temperature which invokes radiative heat transfer. This is also often accompanied by turbulent convection. Examples include prismatic-block type components in high temperature reactors (HTR) [12] wherein excessive decay heat is extracted most efficiently via conduction and radiation from the fuel to the vessel and via radiation and natural convection from the vessel to a water-based circuit positioned on the vault walls. Further nuclear engineering applications of turbulent radiative flows is the Pebble Bed Modular Reactor (PBMR) [13] and sodium pool combustion in fast breeder reactors [14]. Radiative turbulence is also common in fire dynamics [15] and plasma astrophysics [16]. In all these applications, the addition of thermal radiation effects to buoyancy-driven turbulent flow allows for more accurate prediction of heat transfer rates and temperature distributions on solid wall surfaces. In particular, advanced radiative turbulence models can be utilized very effectively to optimize the design of these heat transfer systems in addition to cooling towers and solar collectors. Detailed numerical simulations of turbulent radiative flows therefore play a crucial role in energy transmission between a solid surface and the fluid flowing which enable more robust predictions of thermal transfer rates and energy distributions above the surface of solid geometries.

Turbulent flow has been extensively investigated using a variety of theoretical, experimental and numerical approaches due to its complexity. However no comprehensive established theory currently exists. Although direct computer generation of chaotic flow via Navier-Stokes (NS) equations is theoretically possible, *statistical models* are typically used in practice to reduce computational times. These models rely on *Reynolds decomposition*, which describes a chaotic flow in terms of its average velocity and chaotic intensity components [17]. Many approaches are available for simulating turbulent flows including large eddy simulation (LES), direct numerical simulation (DNS), Monte-Carlo stochastic models, shear-stress transport models (SST) etc. However they are very expensive computationally and require exceptionally powerful hardware. The RANS (Reynolds-averaged N-S equations) procedure is computationally efficient, involving the solution of time-averaged Navier-Stokes equations with semi-empirical turbulence modeling. A Reynolds-averaged chaotic flow simulation employs a statistical model such as the kinetic energy-dissipation (k - ϵ) model, which characterizes chaotic flow using *turbulence energy and dissipation rate as the key*

characteristics, and permits relatively easy enforcement of the boundary conditions. To this end, the low Reynolds number (LRN) k - ϵ model is selected in the present study.

As a foundation for turbulent radiative MHD flow simulation, a number of studies have scrutinized unsteady laminar flows in external boundary layer flows for various geometries with different physical and chemical effects. These studies provide a deep insight into the interaction of multiple physics effects such as magnetic fields, radiation heat transfer, viscous heating, mass transfer, rotation, unsteady flow etc. This then provides a good platform for interpreting more complex turbulent simulations involving these multi-physics effects. In order to investigate the magnetized thermal buoyancy-driven dissipative flow around an isothermal vertical plate under the impact of a uniform transverse magnetic field, Soundalgekar and Takher [18] employed a series solution technique. They observed that the dissipation effects in the flow regime are enhanced by amplifying the Lorentz hydromagnetic body force and the Prandtl number. Ganesan and Rani [19, 20] investigated combined thermo-solutal free convection around a vertical cylinder under a radial magnetic field effect. Reddy *et al.* [21] utilized the Crank-Nicolson finite difference scheme to compute the mixed MHD radiative convective flow from a vertical wall with an energy source/sink. Using the same numerical method, Takhar *et al.* [22] studied the unsteady buoyancy-driven flow along a plate using inconstant surface energy. Additionally, Seth *et al.* [23] found theoretical solutions using the Laplace transformation method for the influence of radiation and rotation impacts on unsteady magneto-convection from an impulsively moving wall with ramped temperature in a porous medium. Poonia and Umashankar [24] reported analytical solutions for impulsive thermal radiative MHD flows in a porous medium with ramped temperature using an analytical solution with homogenous chemical reaction. Mehta and Kataria [25] investigated the energy generation/absorption effect on transient free-driven oscillating magnetized second grade viscoelastic fluid flow with radiative flux and chemical reaction. Many other excellent studies have been communicated by Ullah *et al.* [26], Hasanuzzaman *et al.* [27], Bordoloi *et al.* [28] and Gopal *et al.* [29]. Many of these investigations utilized the Rosseland algebraic flux model which is valid for optically thick “gray” fluids (gases or liquids) in absorbing and emitting but non-scattering conditions.

Turbulent convective flows with thermal radiation or MHD among other effects have also received some attention in recent years. Ji and Gardner [30] utilized the k - ϵ turbulence model to examine electromagnetic and turbulent convective flow in an electrically insulated pipe with a uniform heat flux at the wall, under radial magnetic field, achieving good correlation

experimental results. They showed that magnetohydrodynamic fluxes can be handled by the $k-\varepsilon$ turbulence model and that turbulence suppression is achieved with strong magnetic field intensity, with Lorentz force successfully damping inertial force. Cheng and Miller [31] conducted a numerical and experimental investigation on turbulent free air-driven flow in a vertical rectangular channel with a one-sided heated wall under thermal radiation flux. They assumed the fluid (air) to be radiatively non-participating and the channel walls as grey and diffuse and deployed a surface to surface net-radiation method for enclosures with associated view factors in the FLUTAN CFD code. They noted that higher radiative influx is present at the inlet and outlet regions compared to the core zone due to radiative losses. They further observed that at high wall emissivity, greater heat transfer from the wall is associated with radiation rather than convection. The effect of a magnetic field in turbulence closure models with additional source terms due to Lorentz force was examined by Kenjeres and Hanjalic [32] using the standard LRN $k-\varepsilon$ model. They employed a DNS (direct numerical simulation) approach and simulated the 3-D entry flow of mercury in a rectangular duct under strong transverse magnetic field (Hartmann number of 700). They obtained the experimentally-observed M-shaped velocity profiles and demonstrated that the LRN model is superior to the eddy viscosity turbulence model. They also showed that significant turbulence damping is produced at high magnetic field, and partial re-laminarization is induced. Kobayashi [33] employed subgrid models to linearize turbulent MHD channel flows with a magnetic field perpendicular to the insulated walls at low magnetic Reynolds number. They found that as Lorentz force increases, the natural magnetic chaotic flow transitions to a laminar MHD flow at a critical Hartmann number. Marigi *et al.* [34] used a Reynolds averaged Navier-Stokes (RANS) model to simulate turbulent MHD flow of a rotating fluid past an impulsively started semi-infinite plate using the finite difference method. Kinyanjui *et al.* [35] investigated the turbulent rotating flow from a semi-infinite vertical porous plate in the presence of a variable magnetic field, also with a RANS model, computing the wall momentum and mass transfer rates using Newton's interpolation formula. Gebre *et al.* [36, 37] utilized the RANS model to simulate magnetized turbulent flows from a vertical wall with viscous dissipation, thermal radiation, Ohmic heating and thermal buoyancy effects. Similar studies exploring the collective effects of thermal radiation, magnetic fields, viscosity, porous media drag, mass transfer and rotation about a non-constant vertical porous plate on flow variables using RANS models have been communicated by Ngari *et al.* [38] and Ganga *et al.* [39] (for nanofluids). These studies showed that the average energy distribution decays with an increase in Prandtl and Lewis numbers. Xenos [40] computed the turbulent compressible Reynolds averaged boundary layer

(RABL) convective flow along a wall with the combined effects of magnetic field, thermal radiation, and local wall suction using the Keller box method. He utilized the Baldwin Lomax and extended Kays-Crawford turbulent models for simulating kinematic eddy viscosity and turbulent Prandtl number, respectively. He noted that judicious combinations of thermal radiation flux and magnetic field provide a wall cooling effect and this is amplified for the case of high free-stream temperature. Ochola *et al.* [41] addressed the transient free-driven magnetized turbulent flow with Hall and ion slip currents using a finite difference technique and RANS model. Anvesh and Harish [42] used the Lambremhorst turbulence model and the Chandrasekhar discrete ordinates method (DOM) to compute the radiative turbulent air entering into a convectively heated vertical channel with buoyancy effects. They showed that much greater isotherm magnitudes are computed with radiation for the buoyancy-assisted scenario, and that significant flow acceleration is also induced. Chepkemoui and Mukuna [43] studied the magnetized transient free motion turbulent flow about an infinite heat-absorbing wall with the Prandtl Mixing length model.

Rather than solely analyzing the averaged flow of fluids, *visualization of turbulent flows* is crucial for furnishing a comprehensive understanding of fluid mechanics as the movements of fluids are often invisible to the human eye. To visualize fluid motions and their interactions with surroundings, various innovative techniques have been developed over time. These visualization techniques allow us to observe turbulent flow patterns and gain insight into the theories that can be applied. Thermal radiation is an effective means of optimizing the design of systems that involve solid boundaries and is useful in visualizing turbulence flow patterns around geometric structures. The concepts of heatlines and streamlines are significant contributions to the growth of the theory of single-phase convection energy transfer theory and fluid flow, and they are important tools for visualizing and understanding thermal energy distribution and thermal mixing inside or close to the boundary layer of a given geometry. Although much research has been conducted on heatlines and streamlines in laminar convection flows during the last thirty years, there have been rather limited investigations of their application in turbulent flow visualization. Kimura and Bejan [44] introduced the concept of heat function and heat lines as an alternative to traditional isotherm approaches. This approach has been further developed and extended by several researchers including Littlefield and Desai [45], Aggarwal and Manhapra [46], Morega and Bejan [47] and Costa [48], etc. Similarly, Rani and Reddy [49] conducted heat flow visualization in couple stress fluid convection external to a hollow cylinder. Rani *et al.* [50] computed energy and mass flow

visualizations of a couple stress boundary layer convection adjacent to a hot cylinder using the finite difference Crank-Nicolson method. Further, Reddy *et al.* [51-53] described the heat flow visualization of non-Newtonian fluids, including Casson, micropolar and third-grade fluids, in external boundary layer flows from a cylinder. Tao *et al.* [54] conducted a comprehensive evaluation and comparison of the heat line concept and field synergy principle. Islam *et al.* [55] performed heat line visualization for magnetohydrodynamic natural convective nanofluid in a prismatic enclosure using the Galerkin finite element approach. Furthermore, Kumar and Mondal [56] used Bejan's heat function and finite difference method to visualize the magnetized Casson fluid flow across a wavy wall. Venkatadri *et al.* [57] used both Bejan's heatline method and the Hooman energy flux vector method to visualize radiative flux effects on buoyancy-driven convection in a solar collector enclosure. These studies as elaborated earlier have been confined to laminar rather than turbulent convection flows. However, recently turbulent heat line visualizations have appeared in the literature. Sukanta [58] introduced the concept of turbulent heat function by using a four-equation low Reynolds $k-\epsilon$ algebraic turbulence model without boundary layer approximations to visualize the direction of heat flow along a heated vertical flat plate in a buoyancy-driven turbulent flow. Suresha and Reddy [59] visualized turbulent boundary layer flow along a vertical wall using the LRN kinetic energy and dissipation rate model. Suresha *et al.* [60] utilized Bejan heat and mass line visualization and the LRN $k-\epsilon$ model with a finite difference method for turbulent convective flow. Despite these developments, a scrutiny of the literature has revealed that thus far no studies have reported heatline visualization of magnetohydrodynamic radiative turbulent boundary layer flows. *This is the focus and novelty of the present work in which consider the average heat flow visualization in convective boundary layer flow from a vertical surface with thermal radiation flux and a transverse magnetic field using the LRN $k-\epsilon$ model.* Rosseland's flux model is deployed [57]. While this is a relatively simple radiative model and other more sophisticated flux models are available e.g. Cogley-Vincenti-Giles non-gray gas model [61], Schuster-Schwartzchild 2-flux [62], surface-to-surface (STS) model in ANSYS FLUENT software [63] and the Traugott P1 differential approximation [64], these have generally been deployed in laminar convective-radiative boundary flows only. The present approach is the first step in building more comprehensive numerical models for turbulent radiative flows and therefore Rosseland's model is a good starting point. The governing equations of the fluctuating flow are nonlinear and coupled, and therefore the partial differential conservation equations are discretized with an optimized Crank-Nicolson implicit finite difference scheme. To visualize the turbulent flow, mathematically constructed heat and stream functions are formulated and

solved using a second-order central difference scheme. The computer-generated mean velocity, temperature, kinetic energy, and dissipation rate are studied by varying all the key control factors such as the turbulent Reynolds number (Re_t) magnetic field (M) and thermal radiation (Nr). This paper rigorously visualizes the contours of average velocity, temperature, turbulent kinetic energy, and dissipation rate of kinetic energy, along with heat lines and streamlines for the first time in the presence of magnetohydrodynamic (MHD) body force and radiative heat transfer. Additionally, we demonstrate the difference between laminar and turbulent heat flow visualization using flow field contours. The simulations find important applications in nuclear engineering duct flows and provide a foundation for extension to more complex 3-D visualizations.

2. Statement of the turbulent MHD radiative convective nuclear flow problem:

The effects of thermal radiation and magnetic field on incompressible natural convective Newtonian electro-conductive turbulent flow from a vertical isothermal plate, are studied, as depicted in **Figure 1**. A rectangular geometry is used, with the x -axis along the vertical plate and the y -axis normal to the plate. The free stream mean energy, \bar{T}_∞ , is the stationary surrounding average temperature located away from the solid surface (wall i.e. plate). The initial time is $t' = 0$, and the flow is initiated at $t' > 0$, the average temperature on the plate is $\bar{T}_w (> \bar{T}_\infty)$, and is maintained at the same level for all $t' > 0$. As a result of this mean temperature difference, density variations occur in the turbulent flow regime, which causes the flow to move under the influence of gravitational force in the natural convection process. The transition of average velocity and temperature occurs in a thin layer next to the plate, which is known as the turbulent boundary layer. Under the assumptions and the use of Boussinesq's approximation, the resulting turbulent boundary layer approximations of the average mass, momentum, temperature, turbulence energy and turbulent dissipation rate equations are given by extending the model in Suresha *et al.* [53] to include magnetic Lorentz body force and thermal radiation flux effects:

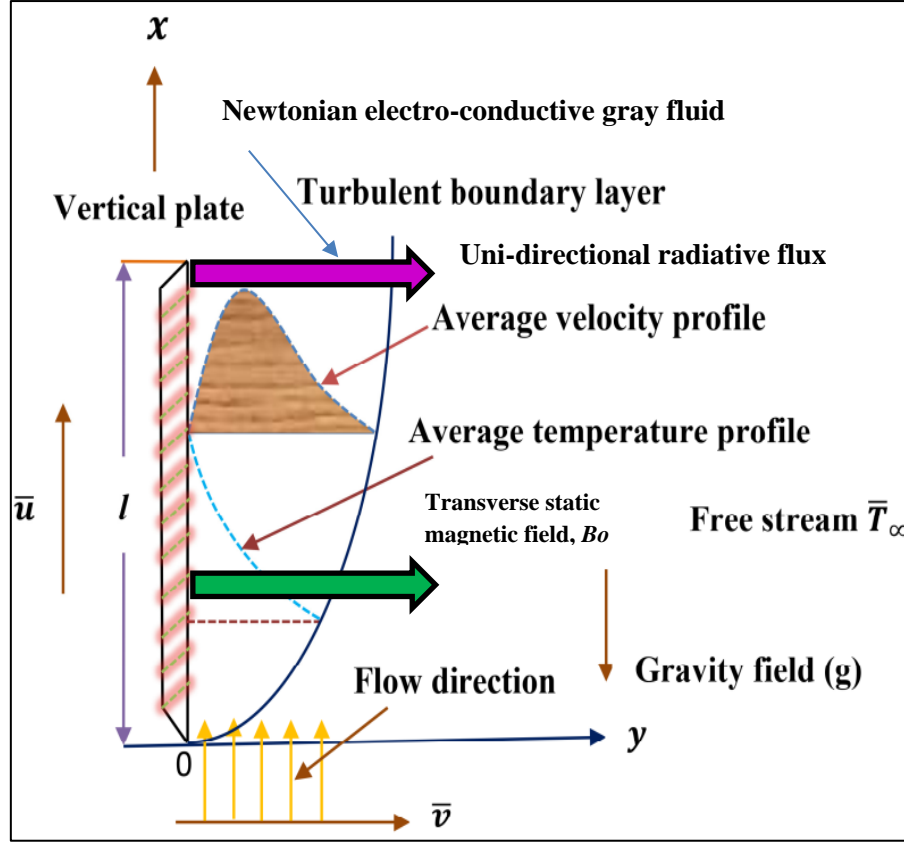


Figure 1: Coordinate system for MHD turbulent radiative boundary layer flow.

2.1 Governing equations of turbulent flow:

Average continuity equation:

$$\frac{\partial \bar{u}}{\partial x} + \frac{\partial \bar{v}}{\partial y} = 0 \quad (1)$$

Average momentum equation:

$$\frac{D\bar{u}}{Dt'} = \frac{\partial}{\partial y} \left[(\nu + \nu_t) \frac{\partial \bar{u}}{\partial y} \right] + g\beta_{\bar{T}}(\bar{T} - \bar{T}_{\infty}) - \frac{\sigma B_0^2 \bar{u}}{\rho} \quad (2)$$

Average energy equation:

$$\frac{D\bar{T}}{Dt'} = \frac{\partial}{\partial y} \left[\left(\nu + \frac{\nu_t}{\sigma_T} \right) \frac{\partial \bar{T}}{\partial y} \right] + \frac{16\sigma_s \bar{T}_{\infty}^3}{\rho c_p k^*} \frac{\partial^2 \bar{T}}{\partial y^2} \quad (3)$$

Typically, turbulence modeling involves the incorporation of eddy viscosity ν_t into the momentum and energy conservation equations (2) and (3). There are various methods for modeling eddy viscosity, such as algebraic methods, k- ϵ , k- ω , and Spalart-Allmaras models. Here we implement the LRN k- ϵ turbulence model due to its computational efficiency and

simplicity. In equations (1)-(3), the turbulent kinematic viscosity (ν_t) is calculated using additional transport equations for turbulence energy (k) and its dissipation rate (ϵ). As there are more unknowns than equations, additional transport equations are necessary to close the turbulence model. The equations for k and ϵ can be derived from the Reynolds decomposition of Navier-Stokes equations [59] and are presented below:

Turbulence energy equation:

$$\frac{Dk}{Dt'} = \frac{\partial}{\partial y} \left[\left(\nu + \frac{\nu_t}{\sigma_k} \right) \frac{\partial k}{\partial y} \right] + \nu_t \left(\frac{\partial \bar{u}}{\partial y} \right)^2 - \epsilon - 2\nu \left(\frac{\partial k^{1/2}}{\partial y} \right)^2 \quad (4)$$

Kinetic energy's dissipation rate equation:

$$\frac{D\epsilon}{Dt'} = \frac{\partial}{\partial y} \left[\left(\nu + \frac{\nu_t}{\sigma_\epsilon} \right) \frac{\partial \epsilon}{\partial y} \right] + C_1 \frac{\epsilon \nu_t f_1}{k} \left(\frac{\partial \bar{u}}{\partial y} \right)^2 - C_2 f_2 \frac{\epsilon^2}{k} + 2\nu \nu_t \left(\frac{\partial^2 \bar{u}}{\partial y^2} \right)^2 \quad (5)$$

Where $\frac{D}{Dt'} = \frac{\partial}{\partial t'} + \bar{u} \frac{\partial}{\partial x} + \bar{v} \frac{\partial}{\partial y}$ is the material derivative.

The expression for eddy viscosity (ν_t) of the turbulent flow in the k- ϵ turbulence model is given by

$$\nu_t = C_\mu \frac{k^2}{\epsilon} f_\mu \quad (6)$$

Further, the LRN k- ϵ turbulence model constants and corresponding values in the Eqs. (1)-(6) are given in the below **Table-1** [59]:

C_μ	C_1	C_2	σ_T	σ_k	σ_ϵ	f_1	f_2	f_μ
0.09	1.45	2.0	0.9	1.0	1.3	1.0	$1 - 0.3 \exp(-Re_t^2)$	$\exp\left(\frac{-2.5}{1 + \frac{Re_t}{50}}\right)$

Table-1: Constants and corresponding values for turbulence model.

The initial and boundary conditions for turbulent energy transfer are given below [59]:

$$\begin{aligned} t' \leq 0; \quad & \bar{u} = 0, \bar{v} = 0, k = 0, \epsilon = 0, \bar{T} = \bar{T}_\infty \text{ for all } x \text{ and } y \\ t' > 0; \quad & \bar{u} = 0, \bar{v} = 0, k = 0, \epsilon = 0, \bar{T} = \bar{T}_w \text{ at } y = 0 \\ & \bar{u} = 0, \bar{v} = 0, k = 0, \epsilon = 0, \bar{T} = \bar{T}_\infty \text{ at } x = 0 \\ & \bar{u} \rightarrow 0, \bar{v} \rightarrow 0, k \rightarrow 0, \epsilon \rightarrow 0, \bar{T} \rightarrow \bar{T}_\infty \text{ as } y \rightarrow \infty \end{aligned} \quad (7)$$

Next, the following dimensionless scaling parameters [65-66] are invoked:

$$X = Gr_t^{-\frac{11}{12}} \frac{x}{l}, \quad Y = \frac{y}{l}, \quad U = \frac{Gr_t^{-\frac{11}{12}} \bar{u} l}{\nu}, \quad V = \frac{\bar{v} l}{\nu}, \quad t = \frac{\nu t'}{l^2}, \quad T = \frac{\bar{T} - \bar{T}_\infty}{\bar{T}_w - \bar{T}_\infty}$$

$$Gr_t = \frac{g\beta_T l^3 (\bar{T}_w - \bar{T}_\infty)}{\nu^2}, K = \frac{kl^2 Gr_t^{-\frac{22}{12}}}{\nu^2}, E = \frac{\epsilon l^4 Gr_t^{-\frac{22}{12}}}{\nu^3}, Pr_t = \frac{\nu}{\alpha_t}, Re_t = \frac{k^2}{\nu \epsilon} \quad (8)$$

$$\frac{\nu_t}{\nu} = C_\mu Re_t \exp\left(\frac{-2.5}{1 + \frac{Re_t}{50}}\right), \quad \alpha_t = \frac{K_T}{\rho C_p}, \quad M = \frac{\sigma B_0^2 l^2}{\rho \nu}, \quad Nr = \frac{k^* K_T}{4\sigma_s \bar{T}_\infty^3}$$

Here all parameters are defined in the notation section. Using Eqn. (8) in Eqs. (1)-(5) & (7), the analogous non-dimensional equations emerge as follows.

$$\frac{\partial U}{\partial X} + \frac{\partial V}{\partial Y} = 0 \quad (9)$$

$$\frac{DU}{Dt} = \left(1 + \frac{\nu_t}{\nu}\right) \frac{\partial^2 U}{\partial Y^2} + Gr_t^{-\frac{1}{12}} T - MU \quad (10)$$

$$\frac{DT}{Dt} = \left[\frac{1}{Pr_t} \left(1 + \frac{4}{3Nr}\right) + \frac{\nu_t}{\nu \sigma_T}\right] \frac{\partial^2 T}{\partial Y^2} \quad (11)$$

$$\frac{DK}{Dt} = \frac{\partial}{\partial Y} \left[\left(1 + \frac{\nu_t}{\nu \sigma_k}\right) \frac{\partial K}{\partial Y} \right] + \frac{\nu_t}{\nu} \left(\frac{\partial U}{\partial Y}\right)^2 - E - 2 \left(\frac{\partial K^{1/2}}{\partial Y}\right)^2 \quad (12)$$

$$\frac{DE}{Dt} = \frac{\partial}{\partial Y} \left[\left(1 + \frac{\nu_t}{\nu \sigma_\epsilon}\right) \frac{\partial E}{\partial Y} \right] + C_1 \frac{E \nu_t}{\nu K} \left(\frac{\partial U}{\partial Y}\right)^2 - C_2 [1 - 0.3 \exp(-Re_t^2)] \frac{E^2}{K} + 2 \frac{\nu_t}{\nu} \left(\frac{\partial^2 U}{\partial Y^2}\right)^2 \quad (13)$$

Where $\frac{D}{Dt} = \frac{\partial}{\partial t} + U \frac{\partial}{\partial X} + V \frac{\partial}{\partial Y}$ is the dimensionless material derivative.

The associated dimensionless initial and boundary conditions become:

$$t \leq 0; \quad T = 0, \quad U = 0, \quad V = 0, \quad K = 0, \quad E = 0 \quad \text{for all } X \text{ and } Y$$

$$t > 0; \quad T = 1, \quad U = 0, \quad V = 0, \quad K = 0, \quad E = 0 \quad \text{at } Y = 0 \quad (14)$$

$$T = 0, \quad U = 0, \quad V = 0, \quad K = 0, \quad E = 0 \quad \text{at } X = 0$$

$$T \rightarrow 0, \quad U \rightarrow 0, \quad V \rightarrow 0, \quad K \rightarrow 0, \quad E \rightarrow 0 \quad \text{as } Y \rightarrow \infty$$

3. Numerical methodology:

3.1 Finite difference discretization

For the discretization of the dimensionless Eqs. (9)-(13), the Crank-Nicolson finite difference method (FDM) is applied which offers exceptional stability and excellent convergence. The algebraic difference equation of the above Eqs. (9) is as follows:

$$\frac{U_{l,m}^{n+1} - U_{l-1,m}^{n+1} + U_{l,m}^n - U_{l-1,m}^n}{2\Delta X} + \frac{V_{l,m}^{n+1} - V_{l,m-1}^{n+1} + V_{l,m}^n - V_{l,m-1}^n}{2\Delta Y} = 0 \quad (15)$$

The finite difference discretization of the momentum equation (10) is given by:

$$\begin{aligned} \frac{U_{l,m}^{n+1} - U_{l,m}^n}{\Delta t} + \frac{U_{l,m}^n}{2\Delta X} (U_{l,m}^{n+1} - U_{l-1,m}^{n+1} + U_{l,m}^n - U_{l-1,m}^n) + \frac{V_{l,m}^n}{4\Delta Y} (U_{l,m+1}^{n+1} - U_{l,m-1}^{n+1} + U_{l,m+1}^n - \\ U_{l,m-1}^n) = \left(1 + \frac{v_t}{v}\right) \left(\frac{U_{l,m+1}^{n+1} - 2U_{l,m}^{n+1} + U_{l,m-1}^{n+1} + U_{l,m+1}^n - 2U_{l,m}^n + U_{l,m-1}^n}{2\Delta Y^2} \right) + \left(\frac{T_{l,m}^{n+1} + T_{l,m}^n}{2} \right) Gr_t^{\frac{1}{12}} - \\ M \left(\frac{U_{l,m}^{n+1} + U_{l,m}^n}{2} \right) \end{aligned} \quad (16)$$

The tridiagonal form of Eqn. (16) is as follows:

$$A_1 U_{l,m-1}^{n+1} + B_1 U_{l,m}^{n+1} + C_1 U_{l,m+1}^{n+1} = D_1 \quad (17)$$

$$\begin{aligned} \text{Here } A_1 = -\frac{V_{l,m}^n \Delta t}{4\Delta Y} - \frac{\Delta t}{2(\Delta Y)^2} \left(1 + \frac{v_t}{v}\right), B_1 = 1.0 + \frac{\Delta t U_{l,m}^n}{2\Delta X} + \frac{\Delta t}{(\Delta Y)^2} \left(1 + \frac{v_t}{v}\right) + \frac{M\Delta t}{2}, C_1 = \frac{V_{l,m}^n \Delta t}{4\Delta Y} - \\ \frac{\Delta t}{2(\Delta Y)^2} \left(1 + \frac{v_t}{v}\right), D_1 = U_{l,m}^n - \frac{\Delta t U_{l,m}^n}{2\Delta X} (U_{l,m}^n - U_{l-1,m}^{n+1} - U_{l-1,m}^n) - \frac{V_{l,m}^n \Delta t}{4\Delta Y} (U_{l,m+1}^n - U_{l,m-1}^n) + \\ \frac{\Delta t}{2(\Delta Y)^2} \left(1 + \frac{v_t}{v}\right) (U_{l,m+1}^n - 2U_{l,m}^n + U_{l,m-1}^n) - \frac{M U_{l,m}^n \Delta t}{2} + \Delta t \left(\frac{T_{l,m}^{n+1} + T_{l,m}^n}{2} \right) Gr_t^{\frac{1}{12}}. \end{aligned}$$

The finite difference discretization of the averaged energy equation (11) takes the form:

$$\begin{aligned} \frac{T_{l,m}^{n+1} - T_{l,m}^n}{\Delta t} + \frac{U_{l,m}^n}{2\Delta X} (T_{l,m}^{n+1} - T_{l-1,m}^{n+1} + T_{l,m}^n - T_{l-1,m}^n) + \frac{V_{l,m}^n}{4\Delta Y} (T_{l,m+1}^{n+1} - T_{l,m-1}^{n+1} + T_{l,m+1}^n - \\ T_{l,m-1}^n) = \left[\frac{1}{Pr_t} \left(1 + \frac{4}{3Nr}\right) + \frac{v_t}{v\sigma_T} \right] \left(\frac{T_{l,m+1}^{n+1} - 2T_{l,m}^{n+1} + T_{l,m-1}^{n+1} + T_{l,m+1}^n - 2T_{l,m}^n + T_{l,m-1}^n}{2\Delta Y^2} \right) \end{aligned} \quad (18)$$

The tridiagonal form of Eq. (18) is then:

$$A_2 T_{l,m-1}^{n+1} + B_2 T_{l,m}^{n+1} + C_2 T_{l,m+1}^{n+1} = D_2 \quad (19)$$

$$\begin{aligned} \text{Here the following definitions apply: } A_2 = -\frac{V_{l,m}^n \Delta t}{4\Delta Y} - \frac{\Delta t}{2(\Delta Y)^2} \left[\frac{1}{Pr_t} \left(1 + \frac{4}{3Nr}\right) + \frac{v_t}{v\sigma_T} \right], B_2 = 1.0 + \\ \frac{\Delta t U_{l,m}^n}{2\Delta X} + \frac{\Delta t}{(\Delta Y)^2} \left[\frac{1}{Pr_t} \left(1 + \frac{4}{3Nr}\right) + \frac{v_t}{v\sigma_T} \right], C_2 = \frac{V_{l,m}^n \Delta t}{4\Delta Y} - \frac{\Delta t}{2(\Delta Y)^2} \left[\frac{1}{Pr_t} \left(1 + \frac{4}{3Nr}\right) + \frac{v_t}{v\sigma_T} \right] \text{ and } D_2 = T_{l,m}^n - \end{aligned}$$

$$\frac{U_{l,m}^n \Delta t}{2\Delta X} (T_{l,m}^n - T_{l-1,m}^{n+1} - T_{l-1,m}^n) - \frac{V_{l,m}^n \Delta t}{4\Delta Y} (T_{l,m+1}^n - T_{l,m-1}^n) + \frac{\Delta t}{2(\Delta Y)^2} \left[\frac{1}{Pr_t} \left(1 + \frac{4}{3Nr} \right) + \frac{\nu_t}{\nu \sigma_T} \right] (T_{l,m+1}^n - 2T_{l,m}^n + T_{l,m-1}^n).$$

The finite difference discretization of the turbulent kinetic energy equation (12) is:

$$\begin{aligned} & \frac{K_{l,m}^{n+1} - K_{l,m}^n}{\Delta t} + \frac{U_{l,m}^n}{2\Delta X} (K_{l,m}^{n+1} - K_{l-1,m}^{n+1} + K_{l,m}^n - K_{l-1,m}^n) + \frac{V_{l,m}^n}{4\Delta Y} (K_{l,m+1}^{n+1} - K_{l,m-1}^{n+1} + K_{l,m+1}^n - \\ & K_{l,m-1}^n) = \left(1 + \frac{\nu_t}{\nu \sigma_k} \right) \left(\frac{K_{l,m+1}^{n+1} - 2K_{l,m}^{n+1} + T_{l,m-1}^{n+1} + K_{l,m+1}^n - 2K_{l,m}^n + K_{l,m-1}^n}{2(\Delta Y)^2} \right) + \frac{\nu_t}{\nu} \left(\frac{U_{l,m+1}^n - U_{l,m-1}^n}{2\Delta Y} \right)^2 - \\ & \left(\frac{E_{l,m}^{n+1} + E_{l,m}^n}{2} \right) - 2 \left(\frac{(K^{1/2})_{l,m+1}^{n+1} - (K^{1/2})_{l,m-1}^{n+1} + (K^{1/2})_{l,m+1}^n - (K^{1/2})_{l,m-1}^n}{4\Delta Y} \right)^2 \end{aligned} \quad (20)$$

The tridiagonal form of Eq. (20) is as follows:

$$A_3 K_{l,m-1}^{n+1} + B_3 K_{l,m}^{n+1} + C_3 K_{l,m+1}^{n+1} = D_3 \quad (21)$$

$$\begin{aligned} \text{Here } A_3 &= -\frac{V_{l,m}^n \Delta t}{4\Delta Y} - \frac{\Delta t}{2(\Delta Y)^2} \left(1 + \frac{\nu_t}{\nu \sigma_k} \right), \quad B_3 = 1.0 + \frac{U_{l,m}^n}{2\Delta X} + \frac{\Delta t}{(\Delta Y)^2} \left(1 + \frac{\nu_t}{\nu \sigma_k} \right), \quad C_3 = \frac{V_{l,m}^n \Delta t}{4\Delta Y} - \\ & \frac{\Delta t}{2(\Delta Y)^2} \left(1 + \frac{\nu_t}{\nu \sigma_k} \right) \quad \text{and} \quad D_3 = K_{l,m}^n - \frac{U_{l,m}^n \Delta t}{2\Delta X} (K_{l,m}^n - K_{l-1,m}^{n+1} - K_{l-1,m}^n) - \frac{V_{l,m}^n \Delta t}{4\Delta Y} (K_{l,m+1}^n - \\ & K_{l,m-1}^n) + \frac{\Delta t}{2(\Delta Y)^2} \left(1 + \frac{\nu_t}{\nu \sigma_k} \right) (K_{l,m+1}^n - 2K_{l,m}^n + K_{l,m-1}^n) + \frac{\nu_t \Delta t}{\nu} \left(\frac{U_{l,m+1}^n - U_{l,m-1}^n}{2\Delta Y} \right)^2 - \\ & \Delta t \left(\frac{E_{l,m}^{n+1} + E_{l,m}^n}{2} \right) - 2\Delta t \left(\frac{(K^{1/2})_{l,m+1}^{n+1} - (K^{1/2})_{l,m-1}^{n+1} + (K^{1/2})_{l,m+1}^n - (K^{1/2})_{l,m-1}^n}{4\Delta Y} \right)^2. \end{aligned}$$

The finite difference discretization of the *dissipation rate* of the turbulent kinetic energy equation (13) is formulated as follows:

$$\begin{aligned} & \frac{E_{l,m}^{n+1} - E_{l,m}^n}{\Delta t} + \frac{U_{l,m}^n}{2\Delta X} (E_{l,m}^{n+1} - E_{l-1,m}^{n+1} + E_{l,m}^n - E_{l-1,m}^n) + \frac{V_{l,m}^n}{4\Delta Y} (E_{l,m+1}^{n+1} - E_{l,m-1}^{n+1} + E_{l,m+1}^n - \\ & E_{l,m-1}^n) = \left(1 + \frac{\nu_t}{\nu \sigma_\epsilon} \right) \left(\frac{E_{l,m+1}^{n+1} - 2E_{l,m}^{n+1} + E_{l,m-1}^{n+1} + E_{l,m+1}^n - 2E_{l,m}^n + E_{l,m-1}^n}{2(\Delta Y)^2} \right) + \\ & C_1 \frac{\nu_t}{\nu} \left(\frac{E_{l,m}^{n+1} + E_{l,m}^n}{2K_{l,m}^n} \right) \left(\frac{U_{l,m+1}^n - U_{l,m-1}^n}{2\Delta Y} \right)^2 - C_2 [1 - 0.3 \exp(-Re_t^2)] \frac{(E_{l,m}^n)^2}{K_{l,m}^n} + \\ & 2 \frac{\nu_t}{\nu} \left(\frac{U_{l,m+1}^n - 2U_{l,m}^n + U_{l,m-1}^n}{(\Delta Y)^2} \right)^2 \end{aligned} \quad (22)$$

The tridiagonal form of Eq. (22) is as follows:

$$A_4 E_{l,m-1}^{n+1} + B_4 E_{l,m}^{n+1} + C_4 E_{l,m+1}^{n+1} = D_4 \quad (23)$$

Where

$$A_4 = \frac{V_{l,m}^n \Delta t}{4\Delta Y} - \frac{\Delta t}{2(\Delta Y)^2} \left(1 + \frac{v_t}{v\sigma_\epsilon}\right), \quad B_4 = 1.0 + \frac{U_{l,m}^n \Delta t}{2\Delta X} + \frac{\Delta t}{(\Delta Y)^2} \left(1 + \frac{v_t}{v\sigma_\epsilon}\right) -$$

$$C_1 \frac{\Delta t v_t}{2\nu K_{l,m}^n} \left(\frac{U_{l,m+1}^n - U_{l,m-1}^n}{2\Delta Y}\right)^2, \quad C_4 = \frac{V_{l,m}^n \Delta t}{4\Delta Y} - \frac{\Delta t}{2(\Delta Y)^2} \left(1 + \frac{v_t}{v\sigma_\epsilon}\right), \quad D_4 = E_{l,m}^n - \frac{U_{l,m}^n \Delta t}{2\Delta X} (E_{l,m}^n - E_{l-1,m}^{n+1} -$$

$$E_{l-1,m}^n) - \frac{V_{l,m}^n \Delta t}{4\Delta Y} (E_{l,m+1}^n - E_{l,m-1}^n) + \frac{\Delta t}{2(\Delta Y)^2} \left(1 + \frac{v_t}{v\sigma_\epsilon}\right) (E_{l,m+1}^n - 2E_{l,m}^n + E_{l,m-1}^n) +$$

$$C_1 \frac{\Delta t v_t E_{l,m}^n}{2\nu K_{l,m}^n} \left(\frac{U_{l,m+1}^n - U_{l,m-1}^n}{2\Delta Y}\right)^2 - C_2 \Delta t [1 - 0.3 \exp(-Re_t^2)] \frac{(E_{l,m}^n)^2}{K_{l,m}^n} +$$

$$2 \frac{\Delta t v_t}{\nu} \left(\frac{U_{l,m+1}^n - 2U_{l,m}^n + U_{l,m-1}^n}{(\Delta Y)^2}\right)^2.$$

The approximated solutions of Eqs. (9)-(14) are obtained in the rectangular region in which $X_{min} = 0$, $X_{max} = 1$, $Y_{min} = 0$ and $Y_{max} = 40$, where Y_{max} corresponding to $Y = \infty$ is located at the edge of the average momentum and temperature turbulent boundary layers. To achieve a steady-state numerical approximation of the average velocity, energy, turbulent kinetic energy (TKE), and dissipation rate of TKE profiles, the initial mesh size was taken as 100×500 . This mesh size varies to the 2nd decimal with that of 50×250 and also a difference in fifth decimal with 200×1000 . Hence, the 100×500 mesh design which achieves grid independence is selected for the current study in which cell sizes of 0.08 and 0.01 along the Y and X paths, respectively. Additionally, $\Delta t = 0.01$ is selected as the time step, which has been tested and provides reliable results. Furthermore, for transient or steady-state solutions of the average turbulent flow variables, an error of less than 10^{-5} is the absolute difference between flow fields at two subsequent time intervals at all mesh nodes. The average temperature field is first determined by solving the energy Eq. (11). Using known values of T , subsequently the velocity U is determined from Eq. (10). Similarly, kinetic energy (K) and dissipation rate (E) are calculated from Eqs. (12) and (13) using the Reynolds averaged Navier-Stokes (RANS) equations (9) and (10).

The finite difference versions of Eqs. (10)-(13) are written in the tridiagonal recurrence three-term form in Eqs.(17), (19), (21) & (23), at $(n + 1)^{th}$ computation. As a result, Eqs.(17), (19), (21) & (23) construct a tridiagonal expression for each inner node at a certain l -level. These equations are solved using the popular Thomas algorithm. In addition, using the given values of U , the velocity, V , is determined directly from Eq. (9). This method continues again for all future l -levels with longer time steps until all mean flow field variables meet the convergence criteria i.e. tolerance level= 10^{-5} .

3.2. Development of turbulent heat and stream functions:

Average heat function:

To derive the turbulent heat function, the average energy equation (3) must be satisfied. Additionally, the net energy flux of the mean flow in the y and x directions can be defined as follows [59]:

$$\frac{\partial \bar{H}}{\partial x} = \rho c_p \bar{v}(\bar{T} - \bar{T}_\infty) - \left(k + \frac{\nu_t}{\sigma_T} \rho c_p + \frac{16\sigma_s \bar{T}_\infty^3}{k^*} \right) \frac{\partial \bar{T}}{\partial y} \quad (24)$$

$$\frac{\partial \bar{H}}{\partial y} = -\rho c_p \bar{u}(\bar{T} - \bar{T}_\infty) \quad (25)$$

It is evident that equations (24) and (25) comply with the steady-state energy equation (3), indicating that they accurately depict the dimensional turbulent heat function $\bar{H}(x, y)$ for natural convective turbulent heat transfer in a Cartesian coordinate system. Hence, equations (24) and (25) can be considered correct representations of the aforementioned function.

Next, we introduce the dimensionless turbulent heat function $H = \frac{\bar{H}}{(\bar{T} - \bar{T}_\infty) Gr_t^{1/2} \left(k + \frac{\nu_t}{\sigma_T} \rho c_p + \frac{16\sigma_s \bar{T}_\infty^3}{k^*} \right)}$ into the above Eqs. (24) and (25) to convert the non-dimensional

turbulent heat function in order that its supreme value is equal to the *overall heat transfer rate of mean flow* on a heated solid wall [46]. Then Eqs. (24) & (25) can be written as follows:

$$\frac{\partial H}{\partial X} = H_T TV - \frac{\partial T}{\partial Y} \quad (26)$$

$$\frac{\partial H}{\partial Y} = -H_T UT \quad (27)$$

where $H_T = \frac{1}{\left(\frac{1}{Pr_t} \left(1 + \frac{4}{3Nr} \right) + \frac{\nu_t}{\nu \sigma_T} \right)}$. Equations (26) and (27) fulfill the dimensionless steady-state

average energy equation (11), confirming that they are correct representations of the dimensionless turbulent heat function $H(X, Y)$ for natural convective turbulent heat transfer in a Cartesian coordinate system. By differentiating equations (26) and (27) with respect to X and Y , respectively, and adding them together, the turbulent heat function (H) can be obtained. The resulting expression is presented below:

$$\frac{\partial^2 H}{\partial X^2} + \frac{\partial^2 H}{\partial Y^2} = H_T \left(T \frac{\partial V}{\partial X} + V \frac{\partial T}{\partial X} - U \frac{\partial T}{\partial Y} - T \frac{\partial U}{\partial Y} \right) - \frac{\partial^2 T}{\partial X \partial Y} \quad (28)$$

Thus, Eq. (28) is the appropriate partial differential equation required to estimate the value of the heat function H throughout the entire turbulent flow domain. It is crucial to compute the average temperature gradient with higher accuracy near the plate since this gradient is directly integrated over the plate height to determine the total average heat

dissipated by the plate. The resulting value is then set as the boundary value of H at the top edge of the plate. Moreover, the value of H at the first grid point near the plate is directly assigned to the plate as $\frac{\partial H}{\partial Y}$ vanishes on a solid wall. The boundary conditions for H can also be obtained from equations (26) and (27) [59].

Average stream function:

Turbulent flow motion can be visualized using the dimensionless turbulent stream function, Ψ , which is obtained by fulfilling the continuity equation (9). In the case of two-dimensional flows, the Cauchy-Riemann equations are used for the turbulent stream function, Ψ and the average velocity components can be expressed as follows:

$$U = \frac{\partial \Psi}{\partial Y}, \quad V = -\frac{\partial \Psi}{\partial X} \quad (29)$$

The above terms in Eq. (29) may be homogenized to yield a single equation which is given below:

$$\frac{\partial^2 \Psi}{\partial X^2} + \frac{\partial^2 \Psi}{\partial Y^2} = \frac{\partial U}{\partial Y} - \frac{\partial V}{\partial X} \quad (30)$$

The values of H and Ψ respectively can be determined by computing the derivatives in equations (28) and (30) using the second-order central difference scheme.

4. Simulated results and discussion:

4.1. Validation:

The obtained time-independent average heat transfer results in the present article are compared with Suresha and Reddy [59] by *ignoring thermal radiation and magnetic field effects i.e. setting $M = 0, Nr = \infty$* . **Table-2** confirms that the current results are proven to match the prior solutions precisely.

Pr_t	Re_t	Temporal maximum time (t) of				Steady- state time (t)	Maximum values at $X =$ 1.0 of		
		U	T	K	E		U	K	E
Suresha and Reddy [59]									
0.71	395	4.56	4.27	4.52	4.63	10.72	0.4890	0.02820	0.1020
7.20	295	4.59	4.30	4.53	4.65	9.28	0.4932	0.0258	0.1107

Present solutions									
0.71	395	4.560	4.271	4.520	4.630	10.720	0.4891	0.02820	0.1021
7.20	295	4.591	4.300	4.530	4.649	9.280	0.4932	0.0257	0.1107

Table-2: Validation of current results with benchmarking to existing result of Suresha and Reddy [59].

4.2. Approximated numerical results:

4.2.1. Impact of magnetic field interaction parameter (M):

Mean velocity:

With the variation of the magnetic field, the simulated average velocity field is pictured in **Fig. 2**. It is perceived from the Fig. 2(a) that initially, all flow fields merged with each other since conduction dominates over convection flow at the position (1, 0.8). After around time $t = 1.0$, the flow field is altered since convection dominates the conduction. Further, the mean velocity commences from zero, attains the maxima with time progression, then decreases, and finally tends to a steady state. Also, steady state mean velocity at $X = 1.0$ is demonstrated in Fig. 2(b) under the influence of a magnetic field. Initially, the turbulent flow field starts from zero near the hot vertical plate, reached its maxima, then asymptotically tends to zero along Y direction. In addition, increasing the magnetic field decreases the average flow field in Fig. 2a,b, *both in time and space*, since increasing the magnetic field enhances the Lorentz magnetic force which counteracts the inertial force. The Lorentz magnetic force induces a damping effects and opposes the motion of charged particles in the electrically conducting fluid. This opposition reduces the velocity fluctuations in the fluid, leading to a decrease in the overall velocity. Turbulent momentum boundary layer thickness will therefore be increased. Turbulence is therefore suppressed with increasing magnetic field intensity. The magnetic interaction parameter, $M = \frac{\sigma B_0^2 l^2}{\rho \nu}$ appears in the Lorentz body force in the dimensionless momentum eqn. (8). Also known as the Stuart magnetic number [67], it expresses the ratio of electromagnetic (Lorentz) force to inertial force. It is also equal to the ratio of the square of the Hartmann number to the Reynolds number. When $M = 0$, the magnetic body force vanishes and both unsteady (Fig. 2a) and steady (Fig 2b) time-mean velocities are clearly maximized. For $M = 2.0$ the Lorentz force is double the inertial force and very quickly the velocity profiles

are stabilized. Chaotic motion is therefore evidently mitigated with strong magnetic field, confirming the trends computed in other studies including Xenos [40]. Since positive values of velocity are sustained in both the unsteady and steady cases, even maximum magnetic field strength does not induce boundary layer flow separation or flow reversal, although coherent turbulent structures will be impeded. In the unsteady case, the oscillations are damped rather quickly after an initial spike with increasing M .

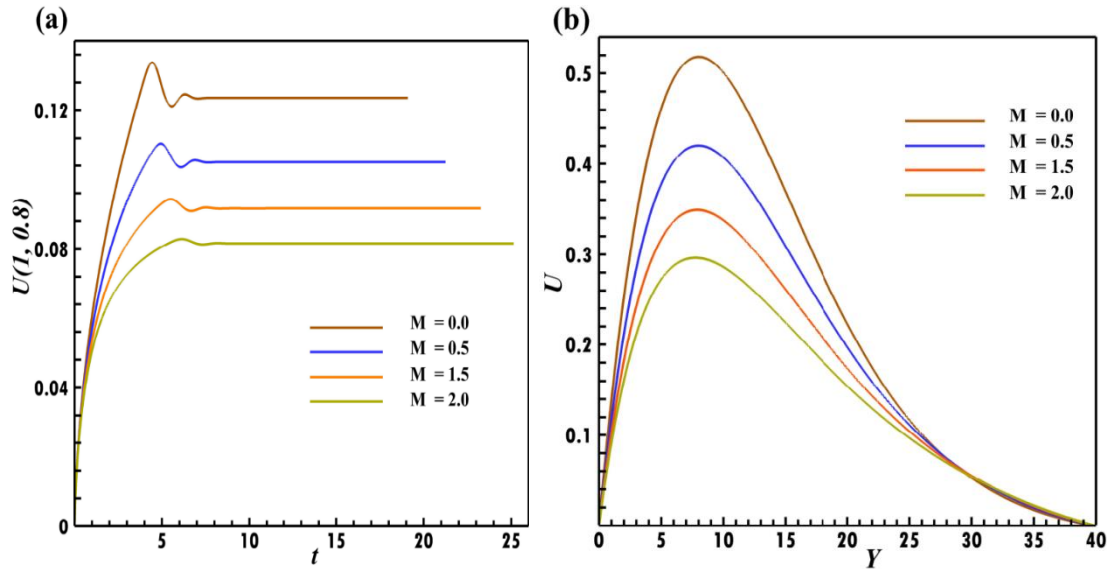


Fig-2. Time-mean velocity field for various values of M at (a) unsteady state; (b) steady state with fixed $Re_t = 500$, $Pr_t = 0.73$, $Gr_t = 1.0$ & $Nr = 1.0$.

Another interesting point is that stronger magnetic field displaces the peak velocity location i.e. more time is needed to attain it in the unsteady case. In the steady case the peak velocity migrates velocity closer to the wall in the which has also been highlighted by Moreau [68]. The smooth steady topologies of velocity at larger times (Fig. 2a) confirm the prescription of a sufficiently large time domain in the computations. Similarly the asymptotically smooth profiles computed with distance, Y , verify that a sufficiently large infinity boundary condition is prescribed in the numerical code.

Mean temperature:

Figure 3a,b display the numerical results for average temperature again over time (Fig. 3a) and space (Fig. 3b) with a variation in magnetic interaction parameter, M . At the position $(1, 0.9)$, Fig. 3(a) demonstrates that mean energy fields accumulate since conduction

dominates convection until $t = 3.0$. The profiles subsequently split into discrete lines with convection dominating. Temperature oscillations are damped rapidly however although they are much larger in the absence of magnetic field ($M = 0$) than when it is present ($M > 0$). Peak temperature is arises quicker for the non-magnetic scenario and is progressively delayed as M increases. Maximum temperature clearly corresponds to the maximum value of magnetic parameter, $M = 2$.

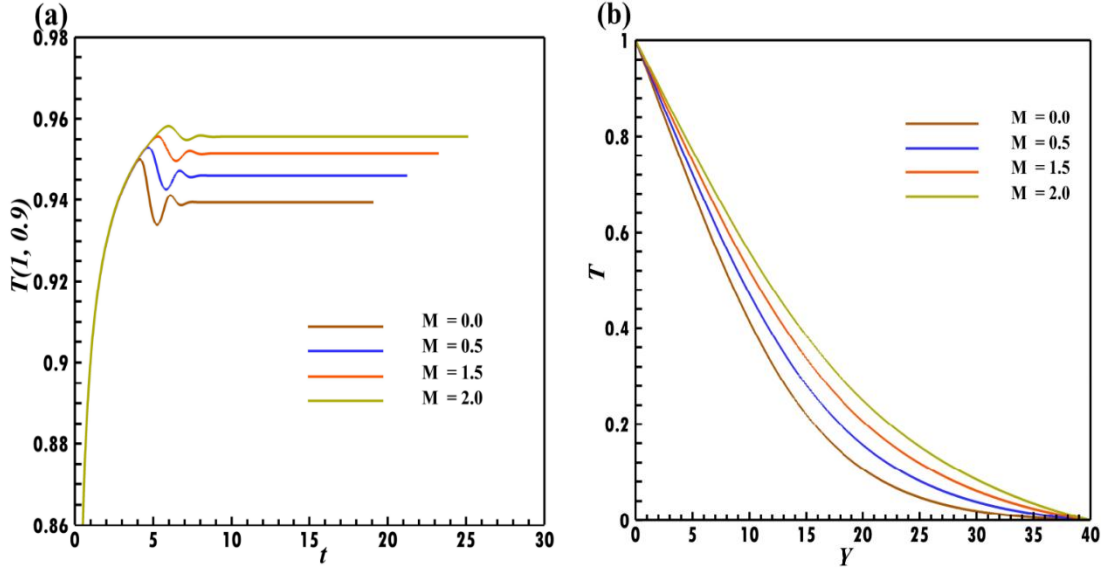


Fig-3. Time-mean energy field for various values of M at (a) unsteady state; (b) steady state with fixed $Re_t = 500$, $Pr_t = 0.73$, $Gr_t = 1.0$ & $Nr = 1.0$.

Turbulent thermal boundary layer thickness will therefore be a maximum for this case whereas it will be minimized for the electrically non-conducting case ($M = 0$). At large times, the chaotic behaviour in temperature is smoothed out and essentially a steady-state condition is achieved for all values of magnetic parameter. However, the *time required to attain this steady state is increased* with enhancing magnetic field. Heating in the turbulent boundary layer is evidently exacerbated with stronger magnetic field. The supplementary work expended by the fluid in dragging against the action of the Lorentz body force is dissipated as heat. This effect is amplified with time initially but stabilized eventually. The time-independent temperature distribution with Y is shown in Fig. 3(b) over the same range of M values as in the unsteady plot (Fig. 3a). Peak temperature always arises at the hot plate wall $X = 1.0$ and monotonically decreases to zero in the free stream. Fig. 3b confirms the classical response in MHD boundary layers, namely that increasing the Lorentz forces enhances the mean temperature profile in the steady state. As noted earlier the friction generated in the fluid due to the work performed

against the magnetic field increases the rate of energy dissipation which in turn elevates thermal boundary layer thickness. In the steady state, this response is sustained at all locations transverse to the hot wall i.e. it is not a localized phenomena.

Dissipation rate of turbulent energy:

The simulated dissipation rate of the kinetic energy profile is portrayed in Fig. 4a,b with reference to **magnetic interaction parameter**, M .

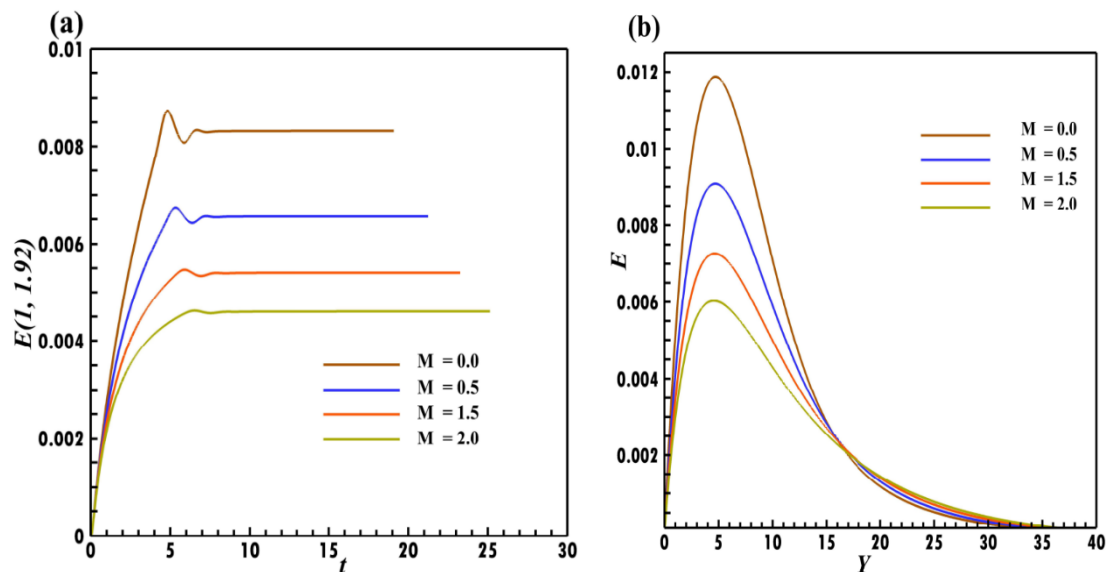


Fig-4. Time-mean **kinetic energy** dissipation rate profile for different values of M at (a) unsteady state; (b) steady state with fixed $Re_t = 500$, $Pr_t = 0.73$, $Gr_t = 1.0$ & $Nr = 1.0$.

It is observed from Fig. 4(a) at $(1, 1.92)$ that the dissipation field ascends rapidly from zero, peaks at a short time thereafter, exhibits a chaotic trend and then eventually tends to the steady state. The oscillatory zones are both compressed and suppressed with stronger magnetic field. Much higher amplitudes of kinetic energy dissipation arise for the non-magnetic case ($M = 0$) and these are significantly damped with increment in magnetic field ($M = 0.5, 1.5, 2.0$). The turbulence suppression associated with magnetic field is therefore again verified. It is also apparent that prior to imposing a magnetic field ($M = 0$), there is a sharp trough and crest computed in the dissipation profile but with the presence of a magnetic field, this is reduced. Further, attaining the steady state increases with the magnifying the magnetic field intensity. In addition, the dissipation field decays with the amplification of the magnetic field since in turbulent flow, the motion of charged particles in the presence of a magnetic field can induce electrical currents, which in turn generate a magnetic field that opposes the original field. This

opposition, known as magnetic damping, leads to the transformation of turbulence energy into thermal energy, resulting in a reduction in the dissipation rate of kinetic energy. The steady-state dissipation rate field is plotted in Fig. 4(b) with the impact of Lorentz force. It shows that initially dissipation rate of the kinetic energy field starts at zero (at the plate surface, $Y = 0$), reaches maxima, then monotonically decreases to zero up to intermediate distance from the wall ($Y = 16$). However thereafter there is a switch-over in the profiles and a weak enhancement in kinetic energy dissipation rate is observed into the free stream.

4.2.2. Impact of turbulent Reynolds number (Re_t):

Turbulent kinetic energy:

Figure 5 a,b illustrates the influence of turbulence Reynolds number on the kinetic energy profile in the turbulent boundary layer region both in time and space. At position (1, 1.92), Fig. 5(a) discloses that the kinetic energy rises from zero by dominating the conduction field; shortly after with convection dominating, the kinetic energy reaches a maximum, then oscillates and profiles all stabilize at large times behaving independently of time. Further, the time required to attain the steady state is amplified with enhancing Re_t . Clearly the contribution of inertial forces relative to viscous forces is enhanced with increment in Re_t . This contributes to the escalation in kinetic energy in the turbulent boundary layer. The time-independent response in kinetic energy to the influence of Re_t is pictured in Fig. 5(b). Inverse parabolic topologies are observed indicating that at the wall and in the free stream the kinetic energy vanishes whereas at intermediate distance from the hot wall it achieves peak magnitude. The profiles are slightly skewed towards the wall with increasing turbulent Reynolds number i.e. the symmetry is warped. Furthermore, the transient kinetic energy profile magnifies with magnifying Re_t parameter over the range 800 to 1200 but thereafter it is reduced. This initial accentuation in kinetic energy is associated with the proliferation in eddies and vortices of varying sizes, velocities, and directions compared to a laminar flow. These eddies and vortices contribute to the kinetic energy of the fluid, and as the Reynolds number increases, the number and intensity of these turbulent motions also increase, hence kinetic energy amplifies. However there is a critical point at which the kinetic energy attained peaks and thereafter with subsequent elevation in turbulent Reynolds number it is reduced (with $Re_t = 1400$). This upper limit to the kinetic energy is associated with a drain in energy available in turbulent flow, which cascades after a threshold, as result of the interplay between inertial and viscous forces, as noted in Cebeci and Smith [69]. The presence of equal electromagnetic and inertial forces ($M = 1.0$)

may also contribute to the damping in kinetic energy at high turbulent Reynolds number, as elaborated by Brandenburg and Dobler [70].

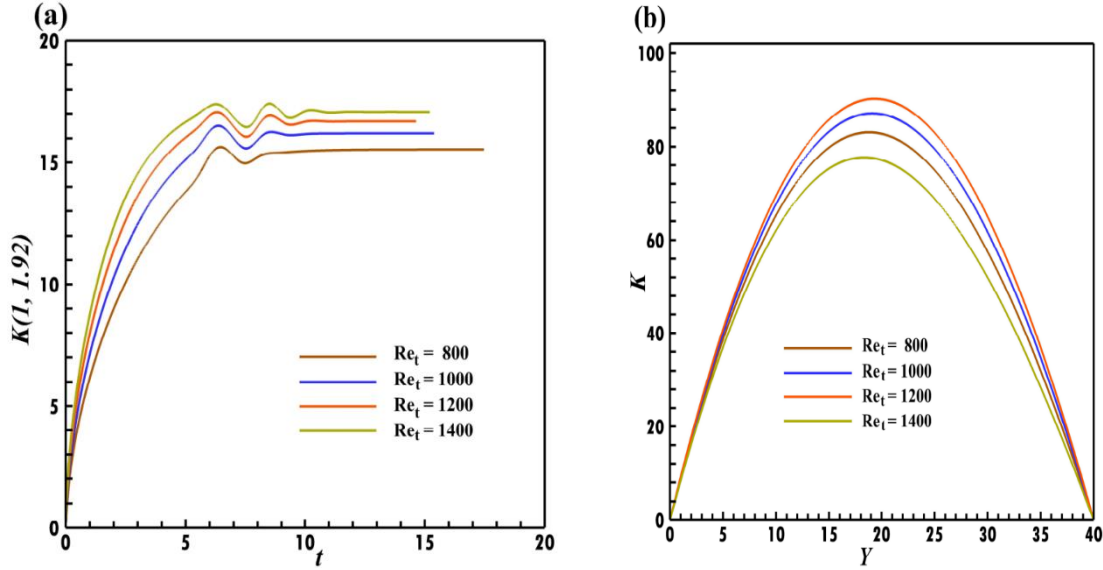


Fig-5. Time-mean kinetic energy profile for different values of Re_t at (a) unsteady state; (b) steady state with fixed $M = 1.0$, $Pr_t = 0.73$, $Gr_t = 1.0$ & $Nr = 1.0$.

4.2.3. Impact of thermal radiation (Nr):

Mean temperature:

Figure 6 a,b depict the simulated average temperature profiles (T) for distinct values of thermal radiation parameter (Nr) in the vicinity of the hot isothermal vertical plate. Fig. 6(a) discloses the transient behavior of the time mean temperature at $(1, 0.9)$. Very sharp oscillations are computed in temperature at small times but these are progressively damped out. From $t \sim 10$, the steady state temperatures are attained and there is a clear depletion in mean temperature with increasing radiation parameter. Nr is also known as the Boltzmann or Stark radiation-conduction parameter. It features in the augmented thermal diffusion term in eqn. (11), viz, $\left[\frac{1}{Pr_t} \left(1 + \frac{4}{3Nr} \right) \right] \frac{\partial^2 T}{\partial Y^2}$. $Nr = \frac{k^* K_T}{4\sigma_s \bar{T}_\infty^3}$ and expresses the relative contribution of *thermal conduction* and *thermal radiation heat transfer*. When $Nr = 1$ both thermal radiation and thermal conduction modes contribute equally. For $Nr \rightarrow \infty$, thermal conduction dominates and thermal radiation heat flux vanishes. In this case, the diffusion term contracts to the classical case of convection-conduction in turbulent boundary layer flow. As Nr is increased the contribution of thermal radiation flux is progressively reduced. Thermal radiation only dominates for $Nr < 1$ whereas it is diminished with $Nr > 1$. The energization of the turbulent shear layer is therefore

decreased with greater values of Nr as observed in Fig 6a,b. The maximum contribution computed for radiative heat transfer is therefore for $Nr = 1$ and this corresponds to the highest unsteady (Fig. 6a) and steady (Fig. 6b) temperatures, although in the latter, very weak elevation is achieved.

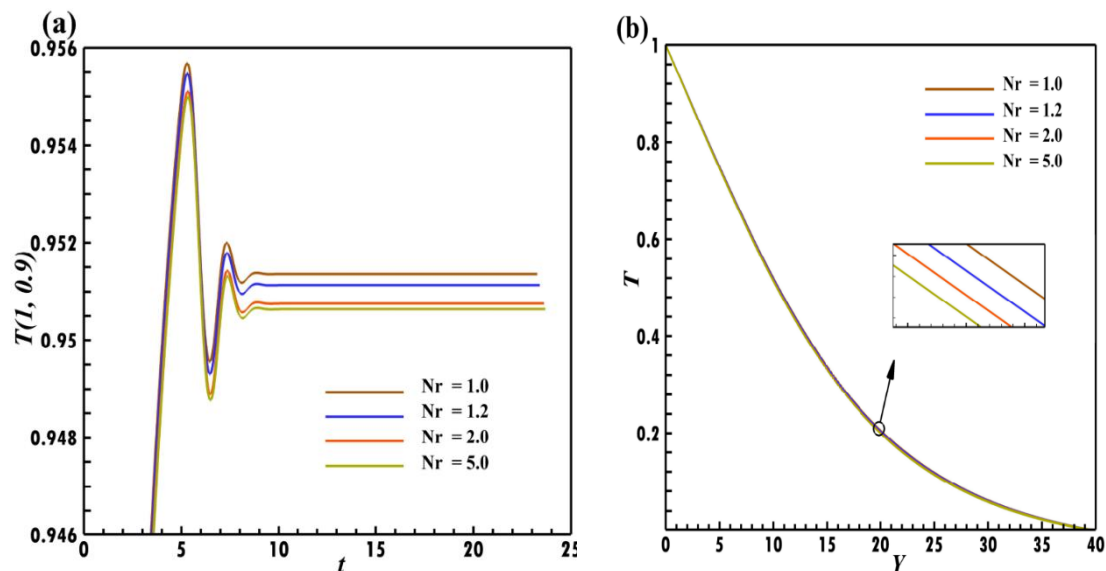


Fig-6. Time-averaged temperature profile for different values of Nr at (a) unsteady state; (b) steady state with fixed $M = 1.0$, $Pr_t = 0.73$, $Gr_t = 1.0$ & $Re_t = 500$.

The modification in temperature is much more dramatic over time compared with distance. The intensification in turbulence may be associated with this effect, as noted in Cheng and Miller [31]. Effectively with time a cooling effect is induced with extraction of radiative heat flux. Thermal boundary layer thickness is therefore depleted with weaker radiative flux ($Nr = 5.0$) compared with stronger radiative flux ($Nr = 1.0$). Furthermore, the presence of turbulence can also affect the temperature profile by enhancing the mixing of fluid particles and in conjunction with the supply of more radiative energy, turbulent thermal boundary layer thickness will be increased. It is also important to note that the inclusion of radiative heat transfer in turbulent simulations offers a more accurate depiction of nuclear reactor duct near-wall flows [4-6]; neglecting of this mode of heat transfer will clearly lead to an underprediction in actual mean temperatures and also thermal boundary layer thickness. Of course the present analysis is restricted to optically dense fluids by virtue of the Rosseland flux approximation. Optical thickness of operational fluids (air, water etc) in nuclear designs is an important parameter to consider since it will influence the distribution of thermal energy in the boundary

layer. In this regard the Traugott P1 differential flux approximation [64] may offer an improved methodology and is under consideration for future studies

4.3. Engineering quantities of interest in laminar and turbulent flows:

The accurate computation of wall skin friction coefficient ($\overline{C_f}$) and Nusselt number (\overline{Nu}) are extremely important in both laminar and turbulent boundary layers [70]. Originating in aerodynamics, these quantities are also critical in nuclear and energy systems design. $\overline{C_f}$ represents the frictional (viscous drag) force per unit area acting on a surface due to the turbulent flow of a fluid. Nusselt number is the ratio of convective heat transfer to conductive heat transfer and also quantifies the rate of heat transmission to the boundary (wall). The accurate evaluation of these dimensionless quantities furnishes excellent insight into the wall characteristics of both laminar and turbulent flows [3,4].

4.3.1. Skin friction coefficient of turbulent flow ($\overline{C_f}$):

The average momentum transfer rate of the turbulent flow from $X = 0.0$ to $X = 1.0$ along the solid plate in dimensionless form is computed as follows [59]:

$$\overline{C_f} = \int_0^1 \left(\frac{\partial U}{\partial Y} \right)_{Y=0} dX \quad (31)$$

Skin friction coefficient profile:

The skin friction coefficient variation with time for both laminar and turbulent flow cases under the effect of magnetic field is portrayed in **Figs. 7(a) & 7(b)** respectively. In both plots similar profiles are computed and the response to increasing magnetic field intensity is the same- i.e. skin friction is damped with stronger magnetic field. The shearing action of the fluid along the plate is therefore significantly suppressed both in laminar and turbulent flow with stronger transverse magnetic field. It is observed from the Fig. 7a that the laminar skin friction coefficient attains the steady state topology more smoothly than the turbulent skin friction in Fig. 7b, which experiences an oscillatory phase at small times but eventually smooths out. The fluctuation in the turbulent case is associated with the chaotic motions at smaller times. These

trends have also been observed by Xenos [40] although he considered compressible flows. Overall, with increasing the magnetic field, the damping action of the Lorentz force suppresses turbulence and reduce momentum transfer at the boundary. Turbulent momentum boundary layer thickness is therefore elevated. Similarly there is a significant increase in laminar boundary layer thickness with stronger magnetic field. The potency of magnetic field application in flow control is therefore clearly demonstrated and has been confirmed in many other studies including Satake *et al.* [9].

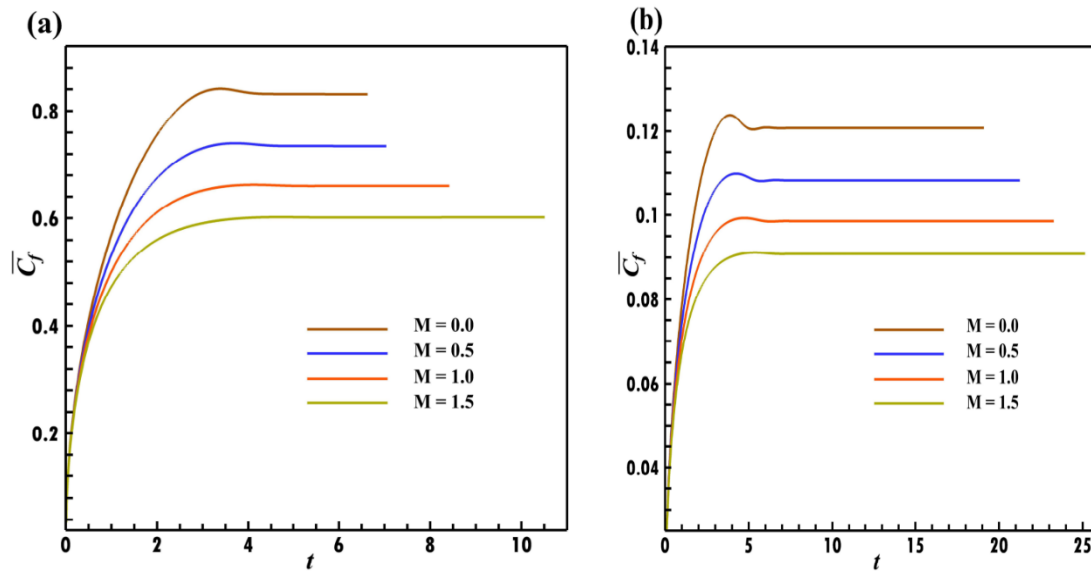


Fig-7. Average momentum profile for different values of M at (a) laminar ($Re_t = 0.0$); (b) turbulent ($Re_t = 500$) with fixed $Nr = 1.0$, $Pr_t = 0.73$ & $Gr_t = 1.0$.

4.3.2. Nusselt number of turbulent flow (\overline{Nu}):

The average heat transfer rate of the turbulent flow from $X = 0.0$ to $X = 1.0$ along the solid plate in dimensionless form is evaluated using the following expression [59]:

$$\overline{Nu} = - \int_0^1 \left(\frac{\partial T}{\partial Y} \right)_{Y=0} dX \quad (32)$$

The integrals in both Eqns. (31) & (32) are calculated using the five-point approximation formula and then computed in MATLAB with the Newton-Cotes integration method.

Nusselt number profile:

The approximated average Nusselt number is visualized in **Fig. 8a,b** with a variation in the magnetic field against time, again for both n laminar and turbulent regimes. It reveals that the turbulent heat transfer decreases with the increasing magnetic field since it is directly connected to the formula \overline{Nu} with a negative sign of temperature profile (Eq. (32)). Also, the magnetic field can suppress heat transfer by reducing the velocity and turbulence intensity of the fluid near the boundary. This trend is consistent with the elevation in temperatures generated with greater magnetic field. This escalation drains heat way from the wall and therefore suppresses the net heat transfer to the wall. This produces the depletion in Nusselt numbers for both laminar and turbulent flow cases.

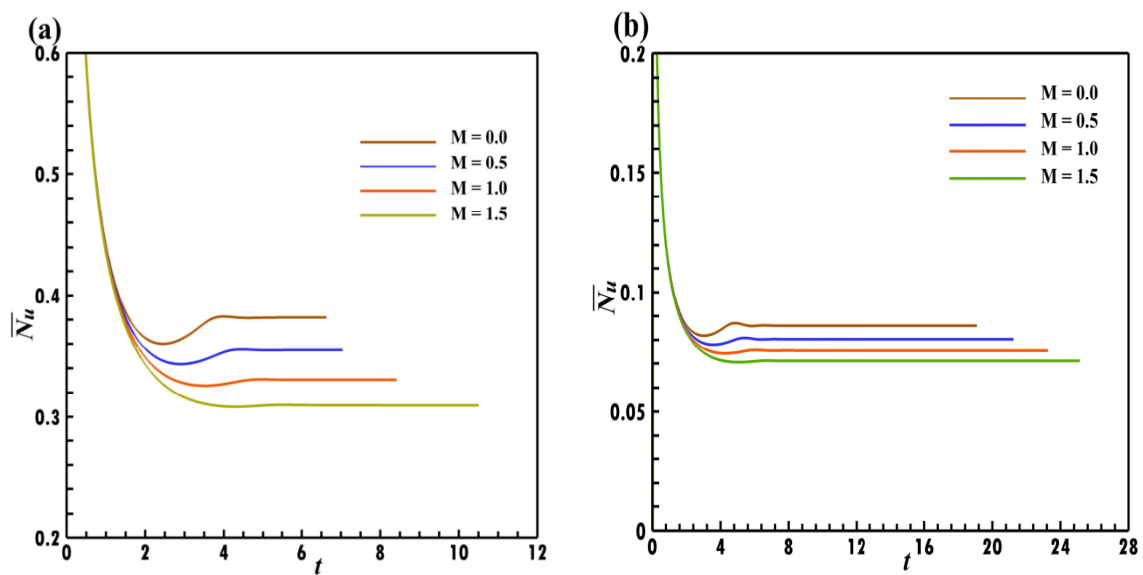


Fig-8. Average heat transfer rate for different values of M at (a) laminar ($Re_t = 0.0$) ; (b) turbulent ($Re_t = 500$) with fixed $Nr = 1.0$, $Pr_t = 0.73$ & $Gr_t = 1.0$.

The energy transfer rate to the wall, is highest at the initial time near the plate, and sharply decreases, eventually tending to a steady state in both regimes. Thermal management at the boundary is therefore very effectively controlled via the mechanism of an external magnetic field which is non-intrusive.

4.4. Visualization of turbulent flow:

4.4.1. Comparison between laminar and turbulent flows:

To convert laminar to turbulent flow, the kinematic viscosity of the turbulent flow, ν_t is considered as zero.

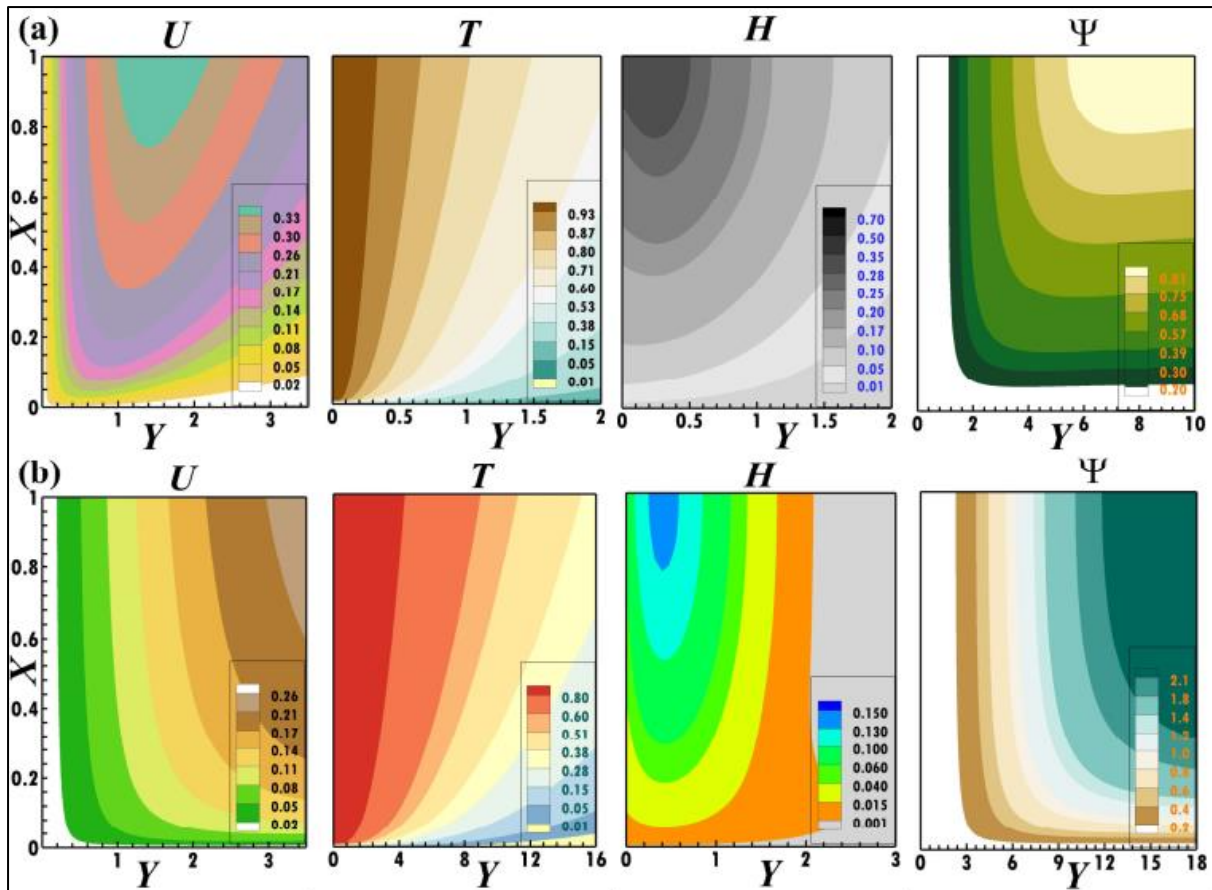


Figure 9: Steady-state contours of velocity (U), temperature (T), streamlines (Ψ), and heat lines (H) for (a) Laminar flow ($Re_t = 0$); (b) Turbulent flow ($Re_t = 500$) with fixed $Pr_t = 0.73$, $M = 1.0$, $Gr_t = 1.0$ & $Nr = 1.0$.

Hence, the simulated magnetized thermal radiative results are studied to compare the laminar (Fig. 9(a)) and turbulent (Fig. 9(b)) cases using the contours of velocity (U), temperature (T), heat (H) and stream (Ψ) lines with varying turbulent Reynolds number (Re_t). It is noticed from the velocity contours (U) of Figs. 9(a) and 9(b) that the velocity contour values of turbulent flow are smaller than laminar flow. Therefore, the velocity magnitudes associated with laminar flow are higher than that of turbulent flow, which is attributable to the much greater energy dissipation due to turbulence. Further, velocity contour lines of turbulent flow are more deviated away from the hot solid vertical wall than that of laminar flow due to fluctuations near the surface- this is confirmed by referring to the velocity contour value 0.26. Wedge topologies are observed for the laminar flow velocity contours which converge towards the lower left corner whereas monotonic bands are associated with the turbulent case emanating from the top left corner and converging in the bottom right corner. It is also noteworthy that these profiles are computed in the presence of intermediate magnetic field ($M = 1.0$), a balance

of thermal buoyancy and viscous forces ($Gr_i = 1.0$) and strong radiative flux ($Nr = 1.0$). Temperature contours (T) in Figs. 9(a) and 9(b) show that energy transfer in the laminar regime is also more intensive than the turbulent regime. There is an intimate interplay between thermal and momentum diffusion in the boundary layer. Since higher velocities are computed for laminar flow (Fig. 9a), the heat transfer in the boundary layer is also enhanced as compared to the turbulent case (Fig. 9b). Also, the temperature contours in the turbulent case deviate more prominently from the heated wall than for the laminar flow case, which can be observed by referring to the contour value 0.05. In accordance with this, the contours of temperature (isotherms) are considerably more clustered around the wall in the laminar case whereas they fan out and are more sparsely dispersed for the turbulent scenario. Further, Figs. 9(a) & 9(b) disclose the distribution of heat function (H) for both laminar and turbulent flows. In close proximity to the hot wall in the laminar regime, the rate of energy transfer is high as compared with the turbulent flow since \overline{Nu} at $Y = 0$ is high for laminar flow as compared with turbulent flow. Also, the contour value 0.1 in heat lines is observed in the turbulent flow at $X = 1.0$ but in the case of laminar flow, it is observed near the leading edge of the plate. Furthermore, in laminar flow, the deviation of energy transfer from the hot vertical wall is greater than that of turbulent flow and this can be analyzed by taking the contour value as 0.1 in both regimes. In addition, heat lines near the hot plate are denser i.e. more constricted, for lesser values of X in the laminar regime and higher values of X in the turbulent regime. Furthermore, turbulent heat lines exhibit stronger curvature and are clustered essentially in the left half space whereas they are more widely dispersed in the laminar case. Inspection of the simulated streamlines (Ψ) for both laminar and turbulent regimes in Figs 9(a) & 9(b) indicates that the laminar streamlines are denser in the region of $1.4 < Y < 2.4$, than those computed for turbulent flow. Additionally, streamlines in the turbulent regime deviate more strongly from the hot vertical solid wall when compared to the laminar regime. This difference can be observed by referring to the contour value of 0.20 in both regimes. Also, the laminar streamlines are denser at the top edge of the plate whereas the turbulent streamlines are denser at the leading edge of the plate.

4.4.2. Contour plots for turbulent flows:

The simulated contours of velocity, energy, kinetic energy, dissipation rate of kinetic energy, heatlines and streamlines for *turbulent flow* with different values of magnetic field (M) are displayed in **Fig. 10**.

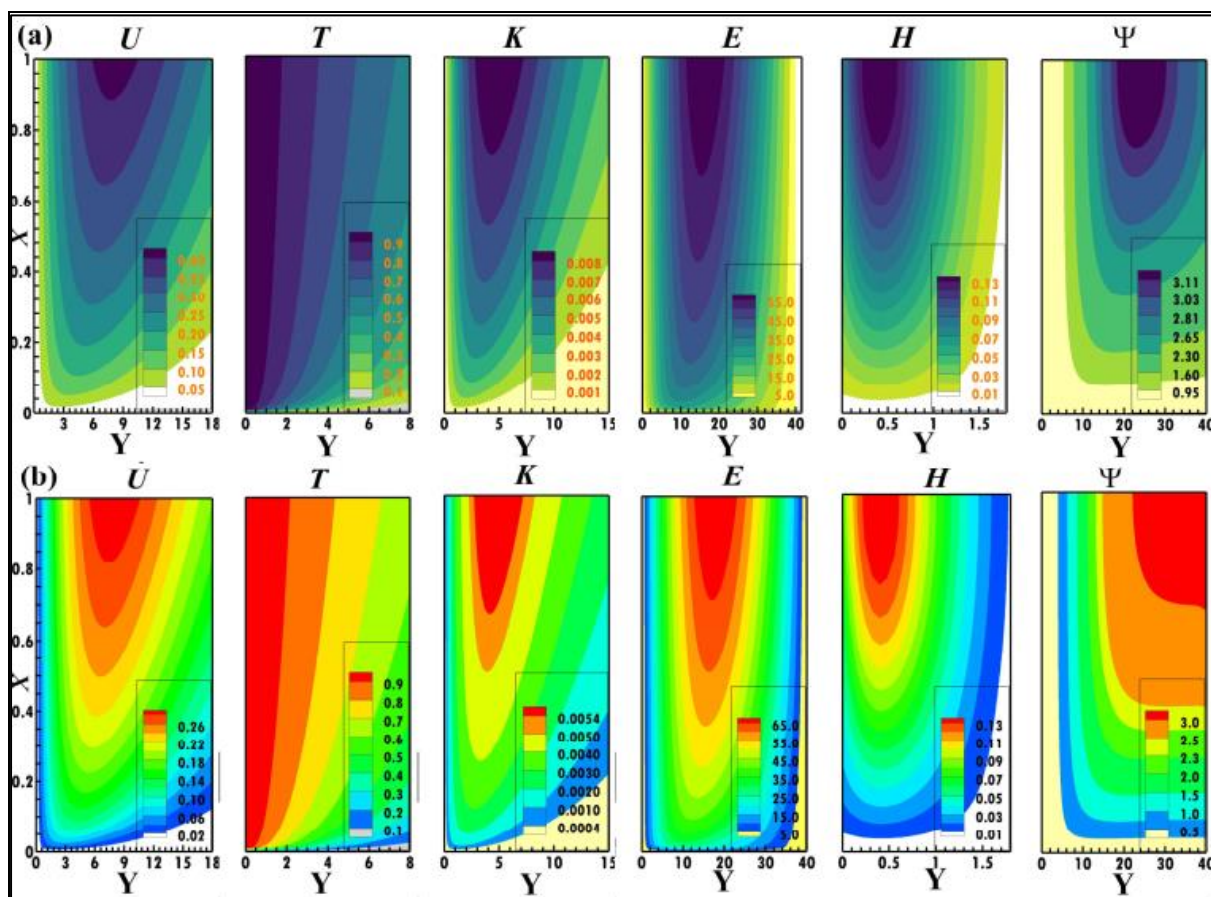


Figure 10: Steady-state contours of velocity (U), temperature (T), kinetic energy (K), dissipation rate (E), heat (H), and stream (Ψ) lines of the turbulent flow at (a) $Re_t = 500$, $M = 0.5$, $Nr = 1.0$; (b) $Re_t = 500$, $M = 1.5$, $Nr = 1.0$ with fixed $Pr_t = 0.73$, $Gr_t = 1.0$.

It is apparent that with higher values of M , the contour values of average velocity diminish and are displaced further from the hot plate due to the action of the electromagnetic Lorentz force. Temperature contours also exhibit some deviation, but this is less pronounced than the disparity in velocity contours. However larger high temperature bands are computed with $M = 1.5$ (Fig. 10a) than with $M = 0.5$ (Fig. 10b) indicating that a heating effect closer to the wall is induced with stronger magnetic field, as observed in earlier graphs. Also contour lines of kinetic energy decrease for raising the values of M since increasing M cause charged particles in the system to move more rapidly, and also overall energy in the system is increased. Further, dissipation rate contour values increased as more energy is being lost from the system, leading to a greater rate of dissipation. Additionally, velocity contours are formed somewhat away from the hot solid wall, whereas kinetic energy and its dissipation rate contours are clustered more densely near the vertical plate. Furthermore, contour plots of heat lines (H) and streamlines (Ψ) displayed allow an examination of heat flux and momentum deviation from the vertical hot

plate. It is observed that variation of streamlines in occurs somewhat further from the hot wall than heat lines due to no-slip condition at the wall and hence the average velocity is small. Overall, the present methodology enables quite clear and comprehensive visualization of turbulent streamlines and isotherms in the magnetized radiative convective turbulent boundary layer regime.

5. Conclusions:

Motivated by studying nuclear engineering near-wall duct transport, a mathematical model has been developed for turbulent hydromagnetic convective boundary layer flow with appreciable radiation heat transfer in the vicinity of a vertical isothermal plate. The transformed non-dimensional governing non-linear and coupled partial differential conservation equations have been solved using an implicit Crank-Nicolson finite difference method (FDM). For the turbulent kinematic viscosity, the LRN $k-\epsilon$ turbulence model has been employed. Rosseland's diffusion algebraic model has been applied for simulating uni-directional radiative transfer for optically dense fluids. Further, the turbulent heat function has been constructed and used to visualize the proper path of turbulent heat flow with thermal radiation and magnetic field effects in the two-dimensional domain. Also, the construction of this turbulent heat function (Eq. 28), enables a more comprehensive visualization of the mean heat flow. The numerical computations for all key variables including velocity, temperature, kinetic energy, dissipation rate, heat function and streamlines, have been displayed via graphs and contour plots for a range of the governing parameters i.e. magnetic interaction parameter, M , radiation-conduction parameter, Nr and turbulent Reynolds number Re_t . Validation of the solutions has been included where possible. The important findings of the current study may be summarized as follows:

- The numerical results show excellent correlation with previous non-magnetic, non-radiative special cases from the literature.
- Average velocity and dissipation rate fields decay whereas the average temperature is strongly amplified with higher magnetic parameter values i.e. stronger Lorentz force.
- Time-mean temperature field is enhanced with stronger thermal radiation parameter (i.e. lower Nr values).

- Visualization of contours reveals that velocity magnitudes associated with laminar flow exceed that of turbulent flow, which is due to the larger energy dissipation due to turbulence.
- Temperature contours (isotherms) are more strongly clustered near the plate in the laminar case whereas they are more sparsely dispersed for the turbulent scenario.
- Near the wall, in the laminar regime, the Nusselt number (heat transfer rate to the wall) exceeds that computed for turbulent flow.
- Very distinct spiked oscillations are observed in temperature at small times but these are progressively damped out with time progression in the turbulent flow.
- Overall significant turbulence suppression is achieved with stronger magnetic field and strong accentuation in heat diffusion and thicker thermal boundary layers are generated with stronger radiative flux primarily for the turbulent flow case.

The present investigation has revealed some interesting characteristics of magnetohydrodynamic radiative turbulent (and laminar) boundary layer flows. Attention has however been restricted to the case of an isothermal vertical wall and Newtonian fluid. Future works may address *non-isothermal flow and also mass diffusion* and additionally examine *non-Newtonian* fluid behaviour, all of which are relevant to nuclear engineering transport phenomena.

References:

- [1] K. Duraisamy, Gianluca Iaccarino and Heng Xiao, Turbulence modeling in the age of data, *Annual Review of Fluid Mechanics*, Vol. 51:357-377 (2019).
- [2] Trevethan M, and Chanson H, Turbulence and turbulent flux events in a small estuary, *Environmental Fluid Mechanics*, 10, 345-368 (2010).
- [3] Harbi A. Daud, Qinling Li, O. Anwar Bég and S.A.A. AbdulGhani, Numerical investigations of wall-bounded turbulence, *Proc. Institution of Mechanical Engineers-Part C: Journal of Mechanical Engineering Science*, 225, 1163-1174 (2011).
- [4] H. A. Daud, Q. Li, O. Anwar Bég and S.A. Ghani, CFD modeling of blowing ratio effects on 3-D skewed gas turbine film cooling, *11th Int. Conf. Advanced Computational Methods and Experimental Measurements in Heat Transfer, Tallinn, Estonia, 14-16 July* (2010).
- [5] A. Derwan, *Tackling Turbulent Flows in Engineering*, Springer, Berlin (2011).
- [6] Hideo Araseki, Shoji Kotake, Numerical method for analysis of turbulent liquid metal magnetohydrodynamic flow, *Nuclear Engineering and Design* 152 (1994) 231-241.

- [7] G. Yagawa, M. Masuda, Finite element analysis of magnetohydrodynamic and its application to lithium blanket design of a fusion reactor, *Nucl. Eng. Des.*, 71 (1982) 121-136.
- [8] Y. Yamamoto et al., DNS and $k-\epsilon$ model simulation of MHD turbulent channel flows with heat transfer, *Fusion Engineering and Design*, 83, 1309-1312 (2008).
- [9] S. Satake, H. Chikamasa, T. Kunugi, K. Takase, Direct numerical simulation of unstable stratified turbulent flow under a magnetic field, *9th Int. Symp. Fusion Nuclear Technology, Oct. 11 -Oct 16, Dalian, China* (2009).
- [10] T. Yokomine, J. Takeuchi, H. Nakaharai, S. Satake, T. Kunugi, N. B. Morley, and M. A. Abdou, Experimental investigation of turbulent heat transfer of high Prandtl number fluid flow under strong magnetic field, *Fusion Sci, and Tech*, 52, 625-629(2007).
- [11] A. Sagara, O. Motojima, K. Watanabe, S. Imagawa, H. Yamanishi, O. Mitarai, T. Sato, H. Chikaraishi, and FFHR Group, Blanket and divertor design for force free helical reactor (FFHR), *Fusion Engineering and Design*, 29 III, 51 (1995).
- [12] J-P. Simoneau *et al.*, Three-dimensional simulation of the coupled convective, conductive, and radiative heat transfer during decay heat removal in an HTR, *Nuclear Engineering and Design*, 237 (2007) 1923-1937.
- [13] J.J. Lee, S.J. Yoon, G.C. Park, W.J. Lee, Turbulence-induced heat transfer in PBMR core using LES and RANS, *J. Nucl. Sci. Technol.*, 44 (7) (2007). 985-996.
- [14] S. Karthikeyan *et al.*, Effect of turbulent natural convection on sodium pool combustion in the steam generator building of a fast breeder reactor, *Nuclear Engineering and Design*, 239 (2009) 2992-3002.
- [15] G. Li, M.F. Modest, Importance of turbulence–radiation interactions in turbulent diffusion jet flames. *ASME J. Heat Transfer*, 125, 831–838 (2003).
- [16] J. Nättilä and A. M. Beloborodov, Radiative turbulent flares in magnetically dominated plasmas, *The Astrophysical Journal*, 921 (2021) 1-30.
- [17] R. Peyret and E. Krause, *Advanced Turbulent Flow Computations*, Springer, USA (2000).
- [18] Soundalgekar V M, and Takhar H S, Dissipation effects on MHD free convection flow past a semi-infinite vertical plate, *Applied Scientific Research*, 36, 163-171(1980).
- [19] Ganesan P, and Rani H P, Transient natural convection along vertical cylinder with heat and mass transfer, *Heat Mass Transfer*, 33, 449-455 (1998).
- [20] Ganesan P, and Rani H P, Unsteady free convection MHD flow past a vertical cylinder with heat and mass transfer. *International J. Thermal Sciences*, 39, 265-272(2000).

- [21] Reddy P B A, Reddy N B, and Palani G, Convective flow past a vertical plate under the influence of magnetic field and thermal radiation subjected to a variable surface temperature in the presence of heat source/sink, *Thermophysics and Aeromechanics*, 19, 489-500 (2012).
- [22] Takhar H S, Ganesan P, Ekambavannan K and Soundalgekar V M, Transient free convection flow past a semi-infinite vertical plate with variable surface temperature, *International Journal Numerical Methods Heat Fluid Flow*, 7, 280-296 (1997).
- [23] Seth, G S, Nandkeolyar R, and Ansari M S, Effects of thermal radiation and rotation on unsteady hydromagnetic free convection flow past an impulsively moving vertical plate with ramped temperature in a porous medium, *Journal of Applied Fluid Mechanics*, 6, 27-38 (2013).
- [24] Ponia and Umashankar, Radiation effect on natural convection flow past an impulsively started infinite vertical plate through porous medium in the presence of magnetic field and first order chemical reaction, *International Journal Applied Mathematics and Statistical Sciences*, 5, 17-28 (2016).
- [25] Mehta R, and Kataria H R, Magnetic field a heat generation effects on second grade fluid flow past an oscillating vertical plate in porous medium, *International Journal Scientific Research in Mathematical and Statistical Sciences*, 7, 1-8 (2020).
- [26] Ullah, M S, Tarammim A, and Uddin M J, A study of two dimensional unsteady MHD free convection flow over a vertical plate in the presence of radiation, *Open Journal Fluid Dynamics*, 11, 20-33(2021).
- [27] Hasanuzzaman M, Ahamed T and Miyara A, Thermal radiation effect on unsteady magneto-convective heat mass transport passing in a vertical permeable sheet with chemical reaction, *Computational and Mathematical Methods in Medicine* (2022).
- [28] Bordoloi R, Chamuah K, and Ahmed N, Free convective MHD radiative flow past a porous vertical plate in a porous medium with chemical reaction, *Biointerface Research Applied Chemistry*, 13, 1-15 (2023).
- [29] Gopal C H K, Sudhakar M, and Rao S M, Unsteady magnetohydrodynamics (MHD) natural convective flow of nanofluids over an infinite perpendicular absorbent plate, *Journal of Nanofluids*, 12, 280-287 (2023).
- [30] Ji H C, and Gardner R A, Numerical analysis of turbulent pipe flow in a transverse magnetic field, *Int. J. Heat Mass Transfer*, 40, 1839-1851 (1997).
- [31] Cheng X, and Miller U, Turbulent natural convection coupled with thermal radiation in large vertical channels with asymmetric heating, *Int. J. Heat Mass Transfer*, 4, 1681-1692 (1998).
- [32] Kenjeres S, and Hanjalic K, On the implementation of effects of Lorentz force in turbulence closure models, *Int. J. Heat Fluid Flow*, 21, 329-337(2000).
- [33] Kobayashi H, Large eddy simulation of magnetohydrodynamic turbulent channel flows with local subgrid-scale model based on coherent structures, *Physics of Fluids*, 18, 045107, (2006).

- [34] Marigi E, Kinyanjui M, and Kwanza J, Hydromagnetic turbulent flow past a semi-infinite vertical plate subjected to heat flux, *Math. Theory and Modelling*, 2 (2012).
- [35] Kinyanjui M, Marigi E M and Kwanza J K, Hydro magnetic turbulent flow of a rotating system past a semi-infinite vertical plate with Hall current, *International J. Pure Applied Mathematics*, 79, 97-119 (2012).
- [36] Gebre D H, Kinyanjui M, and Makinde O D, RANS Modeling of MHD flow over infinite vertical plate in rotating system under the effect of viscous dissipation, Joule heating and radiation, *Int. J. Science and Research*, 3, 1272-1278 (2014).
- [37] Gebre D H, Makinde O D, and Kinyanjui M, Analysis of turbulent Hydromagnetic flow with Radiative heat over a moving vertical plate in a Rotating System, *Applied and Computational Mathematics*, 3,100-109 (2014).
- [38] Ngari D N, Kinyanjui M N, Giterere K, and Kiogora P R, Turbulent hydromagnetic flow with radiative heat over moving vertical porous plate in a rotating system, *International J. Engineering Science and Innovative Technology*, 4 (2015).
- [39] Ganga B, Ansari S M Y, Ganesh N V, and Hakeem A K A, Hydromagnetic flow and radiative heat transfer of nanofluid past a vertical plate, *Journal of Taibah University for Science* (2016). DOI: 10.1016/j.jtusci.2015.12.005.
- [40] Xenos M, Thermal radiation effect on the MHD turbulent compressible boundary layer flow with adverse pressure gradient, heat transfer and local suction, *Open J. Fluid Dynamics*, 7, 1-14 (2017).
- [41] Ochola N J, Awuor K O, Abonyo J O, and Kimathi M E M, Heat and mass transfer past a semi-infinite vertical porous plate in MHD flows in turbulent boundary layer, *World J. Research Review*, 6, 45-63 (2018).
- [42] Anvesh T and Harish R, Radiation effects on turbulent heat transfer characteristics in vertical channel, *Int. J. Recent Tech. Eng.*, 9, 2783-2787 (2020).
- [43] Chepkemoi E, and Mukuna W O, Hydromagnetic free convection unsteady turbulent fluid flow over a vertical infinite heat absorbing plate, *IOSR J. Mathematics*, 17, 42-48 (2021).
- [44] Kimura S, and Bejan A, The heatline visualization of convective heat transfer, *ASME J. Heat Transfer*, 105, 916-919 (1983).
- [45] Littlefield D, and Desai P, Buoyant laminar convection in a vertical cylindrical annulus, *ASME J. Heat Transfer*, 108, 814-821 (1986).
- [46] Aggarwal S K, and Manhapra A, Use of heatlines for unsteady buoyancy-driven flow in a cylindrical enclosure, *ASME J. Heat Transfer*, 111, 576-578 (1989).
- [47] Morega A M, and Bejan A, Heatline visualization of forced convection boundary layers, *Int. J. Heat Mass Transfer*, 36, 3957-3966 (1993).

- [48] Costa V A F, Heatline and mass line visualization of laminar natural convection boundary layers near a vertical wall, *Int. J. Heat Mass Transfer*, 43, 3765-3774 (2000).
- [49] Rani H P, and Reddy G J, Heatline visualization for conjugate heat transfer of a couple stress fluid from a vertical slender hollow cylinder, *Int. Comm. Heat Mass Transfer*, 48, 46-52 (2013).
- [50] Rani H P, Reddy G J, Kim C N, and Rameshwar Y, Transient couple stress fluid past a vertical cylinder with Bejan's heat and mass flow visualization for steady state, *ASME J. Heat Transfer*, 137, 032501 (2015).
- [51] Reddy G J, Kethireddy B, and Bég O. Anwar, Flow visualization using heat lines for unsteady radiative hydro magnetic micropolar convection from a vertical slender hollow cylinder, *Int. J. Mechanical Sciences*, 140, 493-505 (2018).
- [52] Reddy G J, Hiremath A, and Kumar M, Computational modelling of unsteady third-grade fluid flow over a vertical cylinder: A study of heat transfer visualization, *Results in Physics*, 8, 671-682 (2017).
- [53] Reddy G. J., Kethireddy, B, Umavathi, J C, and Sheremet, M A, Heat flow visualization for unsteady Casson fluid past a vertical slender hollow cylinder, *Thermal Science and Engineering Progress*, 5, 172-181 (2018).
- [54] Tao W Q, He Y L, and Chen L, A comprehensive review and comparison on heatline concept and field synergy principle, *Int. J. Heat Mass Transfer*, 135, 436-459 (2019).
- [55] Islam T, Nuralam M, Asjad M I, Parveen N, and Chu Y M, Heatline visualization of MHD natural convection heat transfer of nanofluids in a prismatic enclosure, *Scientific Reports*, 11, 10972 (2021).
- [56] Kumar M, and Mondal P K, Bejan's flow visualization of buoyancy-driven flow of a hydro magnetic Casson fluid from an isothermal wavy surface, *Physics of Fluids*, 33, 093113 (2021).
- [57] K. Venkatadri, O. Anwar Bég, P. Rajarajsweri and V. R. Prasad, Numerical simulation of thermal radiation influence on natural convection in a trapezoidal enclosure: heat flow visualization through energy flux vectors, *Int. J. Mechanical Sciences*, 171, 105391 (2020).
- [58] Sukanta K D, Heatline visualization in turbulent flow, *Int. J. Numerical Methods Heat Fluid Flow*, 6, 37-46 (1996).
- [59] Suresha S P, and Reddy G J, Natural convective turbulent heat flow visualization around a vertical plate using low Reynolds number k- ϵ model, *Waves in Random and Complex Media*, DOI: 10.1080/17455030.2022.2163061 (2023).
- [60] Suresha S P, Reddy G J, and Basha H, Bejan's numerical heat and mass flow visualization in turbulent boundary layer regime, *Waves in Random and Complex Media*, DOI: 10.1080/17455030.2023.2178237 (2023).

- [61] H.S. Takhar, O. Anwar Bég and M. Kumari, Computational analysis of coupled radiation convection dissipative flow in a porous medium using the Keller-Box implicit difference scheme, *Int. J. Energy Research*, 22,141-159 (1998).
- [62] S. Kuharat, O. Anwar Bég, Ali Kadir and B. Vasu, Computation of metallic nanofluid natural convection in a two-dimensional solar enclosure with radiative heat transfer, aspect ratio and volume fraction effects, *Arabian J. Science and Engineering*, 45, 9075–9093 (2020).
- [63] S. Kuharat, O. Anwar Bég, B. Vasu, Ali Kadir, Tasveer A. Bég, H.J. Leonard, W.S. Jouri and J.C. Umavathi, Numerical study of buoyancy-driven convection in a trapezoidal solar enclosure with zinc and diamond nanoparticles, In “*Energy Conversion and Green Energy Storage*”, CRC/Taylor and Francis, USA Eds. (A. Soni, D. Tripathi, J. Sahariya & K. N. Sharma), September (2022).
- [64] O. Anwar Bég, N. Ali, A. Zaman, Eemaan T. A. Bég and A. Sohail, Computational modelling of heat transfer in annular porous medium solar energy absorber with a P1-radiative differential approximation, *J. Taiwan Inst. Chemical Eng.*, 66, 258-268 (2016).
- [65] Reddy G J, Basha H, and Narayanan N S V, Finite difference analysis of unsteady natural convection properties of carbon dioxide in the supercritical region using the Redlich-Kwong equation of state, *Journal of Physics Chemistry Solids*, 122, 284-301(2018).
- [66] Palaiah S S, Basha H, and Reddy G J, Magnetized couple stress fluid flow past a vertical cylinder under thermal radiation and viscous dissipation effects, *Nonlinear Engineering*, 10,343-362 (2021).
- [67] D. Lee; H. Choi Magnetohydrodynamic turbulent flow in a channel at low magnetic Reynolds number, *Journal of Fluid Mechanics*, 439, 367–394 (2001).
- [68] R. Moreau: *Magnetohydrodynamics*, Kluwer Academic Publishers, Dordrecht, Netherlands (1990).
- [69] T. Cebeci, A.M.O. Smith, *Analysis of Turbulent Boundary Layers*, Academic Press, New York (1974).
- [70] Brandenburg, A. and Dobler, W. Hydromagnetic turbulence in computer simulations. *Computer Physics Communications*, 147, 471-475 (2002).